



NRL/MR/7160--20-10,043

Bio-inspired Echolocation Using Characteristics of Propeller System Acoustic Signature

J. LINGEVITCH

W. CALKINS

*Acoustic Signal Processing and Systems, Physical Acoustics Branch
Acoustics Division*

J. GEDER

*Laboratory for Propulsion, Energetic and Dynamic Systems
Laboratories for Computational Physics and Fluid Dynamics*

D. SOFGE

D. LOFARO

L. MCGUIRE

*Navy Center for Applied Research in Artificial Intelligence Branch
Information Technology Division*

M. KELLY

*Offboard Countermeasures Branch
Tactical Electronic Warfare Division*

May 26, 2020

DISTRIBUTION STATEMENT A: Approved for public release; distribution unlimited.

REPORT DOCUMENTATION PAGE

Form Approved
OMB No. 0704-0188

Public reporting burden for this collection of information is estimated to average 1 hour per response, including the time for reviewing instructions, searching existing data sources, gathering and maintaining the data needed, and completing and reviewing this collection of information. Send comments regarding this burden estimate or any other aspect of this collection of information, including suggestions for reducing this burden to Department of Defense, Washington Headquarters Services, Directorate for Information Operations and Reports (0704-0188), 1215 Jefferson Davis Highway, Suite 1204, Arlington, VA 22202-4302. Respondents should be aware that notwithstanding any other provision of law, no person shall be subject to any penalty for failing to comply with a collection of information if it does not display a currently valid OMB control number. **PLEASE DO NOT RETURN YOUR FORM TO THE ABOVE ADDRESS.**

1. REPORT DATE (DD-MM-YYYY) 26-05-2020			2. REPORT TYPE NRL Memorandum Report		3. DATES COVERED (From - To) January 1 – September 30, 2019	
4. TITLE AND SUBTITLE Bio-inspired Echolocation Using Characteristics of Propeller System Acoustic Signature					5a. CONTRACT NUMBER	
					5b. GRANT NUMBER	
					5c. PROGRAM ELEMENT NUMBER	
6. AUTHOR(S) J. Lingeitch, W. Calkins, J. Geder, D. Sofge, D. Lofaro, L. McGuire, and M. Kelly					5d. PROJECT NUMBER	
					5e. TASK NUMBER	
					5f. WORK UNIT NUMBER 1X04	
7. PERFORMING ORGANIZATION NAME(S) AND ADDRESS(ES) Naval Research Laboratory 4555 Overlook Avenue, SW Washington, DC 20375-5320					8. PERFORMING ORGANIZATION REPORT NUMBER NRL/MR/7160--20-10,043	
9. SPONSORING / MONITORING AGENCY NAME(S) AND ADDRESS(ES) Naval Research Laboratory 4555 Overlook Avenue, SW Washington, DC 20375-5320					10. SPONSOR / MONITOR'S ACRONYM(S) NRL	
					11. SPONSOR / MONITOR'S REPORT NUMBER(S)	
12. DISTRIBUTION / AVAILABILITY STATEMENT DISTRIBUTION STATEMENT A: Approved for public release; distribution unlimited.						
13. SUPPLEMENTARY NOTES						
14. ABSTRACT Many species of bats are well-known for their abilities to perceive and navigate environments using sound. While these organisms emit sounds through voice calls and tongue clicks, and traditional engineered systems have looked at dedicated hardware for producing similar signals, the research outlined here seeks to leverage the acoustics inherent in small unmanned aircraft system (UAS) propulsion and control systems hardware to enable localization and navigation tasks. This approach to echolocation reduces size, weight and power requirements, leading to more efficient UAS platforms, among other advantages. Conducting experiments with propellers from hover-capable air vehicles, we have identified the potential utility of using the motor update rate on each of the propeller motors as controllable acoustic signaling devices, demonstrating high signal-to-noise intensity at various specified update frequencies. Further, we have analyzed broadband acoustic data under various propeller operating conditions in the presence of multiple wall configurations. Overall, identification of localization performance limits will help determine the utility of using propeller system embedded acoustics as a navigation tool for small UASs.						
15. SUBJECT TERMS						
16. SECURITY CLASSIFICATION OF:			17. LIMITATION OF ABSTRACT	18. NUMBER OF PAGES	19a. NAME OF RESPONSIBLE PERSON	
a. REPORT	b. ABSTRACT	c. THIS PAGE			Joe F. Lingeitch	
Unclassified Unlimited	Unclassified Unlimited	Unclassified Unlimited	Unclassified Unlimited	51	19b. TELEPHONE NUMBER (include area code) (202) 404-4820	

This page intentionally left blank.

CONTENTS

EXECUTIVE SUMMARY.....	E-1
1. INTRODUCTION	1
2. FREE-FIELD MOTOR NOISE CHARACTERIZATION	2
2.1 8 mm motor - June 14, 2019	3
2.2 8.5 mm motor - February 28, 2019.....	5
2.3 8 mm motor - August, 15 2019	8
3. MOTOR SELF-NOISE IN THE PRESENCE OF A REFLECTING WALL	9
3.1 Model for a broadband interference pattern.....	11
3.2 Example with a known free-field source power spectrum	12
3.3 Cross-correlation processing.....	12
4. CONCLUSIONS.....	15
ACKNOWLEDGMENTS	29
REFERENCES	29
APPENDIX A—Modeling Attenuation.....	31
APPENDIX B—Measurement Summary	33
B.1 January 22, 2019 - 6 mm motor tests	33
B.2 January 24, 2019 - 6 mm motor tests	33
B.3 January 25, 2019 - 4 and 8 mm motor tests	34
B.4 February 25, 2019, 8.5 mm motor measurements	35
B.5 February 27, 2019, 4 mm, 6 mm and 8 mm motor measurements.....	37
B.6 February 28, 2019, 8.5 mm motor measurements	40
B.7 April 9, 2019, 4 mm motor measurements	41
B.8 April 10 - 11, 2019, 4 mm and 8.5 mm motor measurements	43
B.9 June, 14 2019 - 8 mm motor tests	43
B.10 August, 14 2019 - 8 mm motor tests.....	44
B.11 August, 15 2019 - 8 mm motor tests.....	44

FIGURES

1	Photo of 3D printed motor support, and nearby microphones	3
2	Linear microphone array	4
3	Short-time power spectral density, 8 mm motor	5
4	Short-time power spectral density, 8 mm motor, zoomed in	6
5	Time-averaged power spectral density	7
6	Comparison of acoustic power spectral density with PWM signal and motor rotation rate harmonics	8
7	Power spectral density for linear PWM frequency sweep	9
8	Power spectral density for slow duty cycle sweep	10
9	Photo and diagram of 6-channel circular array with motor at center	16
10	Inter-channel comparison of motor noise PSD on circular array at fixed microphone stations..	17
11	Inter-station comparison of motor noise PSD on circular array at fixed microphone channels..	18
12	Inter-channel comparison of ambient noise PSD on circular array at fixed microphone stations	19
13	Inter-station comparison of ambient noise PSD on circular array at fixed microphone channels	20
14	2D motor/microphone geometry	21
15	Interference amplitude	22
16	Measured interference pattern from wall/no-wall power spectral density difference	23
17	Photo of 8-channel array between removable wall and motor	24
18	8-channel array, measured interference pattern from wall/no-wall power spectral density difference	25
19	8-channel array, time delay distance estimation	25
20	2-channel generalized cross-correlation applied to no wall and wall present data	26
21	2-channel generalized cross-correlation processor	27
22	2-channel cross-channel spectral density distance estimation	28
A1	Absorption coefficient	31
A2	Signal to noise ratio attenuation with distance	32

TABLES

B1	January 22, 2019 acoustic measurements.....	33
B2	January 24, 2019 acoustic measurements.....	34
B3	January 25, 2019 8mm motor acoustic measurements	34
B4	January 25, 2019 4 mm motor measurements	35
B5	February 25, 2019 8.5 mm motor tachometer measurements.....	35
B6	February 25, 2019 8.5 mm motor acoustic measurements	36
B7	February 27, 2019 6 mm motor tachometer measurements	37
B8	February 27, 2019 6 mm motor acoustic measurements	37
B9	February 27, 2019 8 mm motor tachometer measurements	37
B10	February 27, 2019 8 mm motor acoustic measurements	38
B11	February 27, 2019 4 mm motor tachometer measurements	38
B12	February 27, 2019 4 mm motor acoustic measurements	39
B13	February 28, 2019 with wall perpendicular to array axis (left column) an no-wall (right column) measurements	40
B14	February 28, 2019 with wall parallel to array axis	40
B15	February 28, 2019 PWM sweeps	40
B16	February 28, 2019 duty cycle sweeps	41
B17	April 9, 2019 PWM and duty cycle sweeps without wall.....	41
B18	April 9, 2019 wall tests	42
B19	June 14, 2019 measurements	43
B20	August 14, 2019 measurements.....	44
B21	August 15, 2019 measurements.....	45

This page
intentionally
left blank

EXECUTIVE SUMMARY

Within the construct of the US-UK Genesis II program, an international cross-service (Air Force Research Laboratory, Naval Research Laboratory, and Defence Science and Technology Laboratory) team was assembled to investigate biomimetic approaches for sensing, guidance, and control paradigms inspired by biological systems using acoustic return signatures from the propulsion systems of micro air vehicles (MAVs). This report describes the year-one acoustic measurements of micro air vehicle motor/propeller systems performed at the NRL Laboratory for Autonomous Systems Research (LASR) facility by the NRL team to determine intrinsic acoustic characteristics useful for navigation and communications.

Analyzing data from multiple motors and motor operating conditions, and with different microphone array configurations, we have identified features in the acoustic signatures that can be exploited for localization and navigation tasks. These features include frequencies associated with motor update rate and duty cycle, as well as interference patterns that result from the presence of reflective objects. We have demonstrated that acoustic interference patterns can be used to detect and compute a relative distance to a wall surface by several related methods using a single or multiple microphone channels. Our first-year results suggest several promising areas for future developments that may be useful in developing extended range object detection capabilities. Following on this work, we are developing algorithms for relative wall position control using real-time feedback of acoustic data produced from the motor propeller system, and investigating machine learning techniques for more advanced on-board processing of acoustic data. Data collected in these measurements was shared through the project agreement with team members at the Air Force Research Laboratory for analysis using topological data analysis on a common data set.

This page
intentionally
left blank

BIO-INSPIRED ECHOLOCATION USING CHARACTERISTICS OF PROPELLER SYSTEM ACOUSTIC SIGNATURE

1. INTRODUCTION

In nature, acoustic sensing is used in many tasks including localization, collision avoidance, navigation, and hunting. Prime examples of in-air echolocation, a form of acoustic sensing using reflected sound to locate objects, can be observed in many bat species whose other senses, such as sight and smell, pale in comparison to that of their mammalian counterparts. By exploiting their unique echolocation capabilities, it has been shown that these bats are able to locate and track prey, and also acquire and internally reconstruct a high-resolution map of their surroundings for navigation. This is possible because of the unique acoustic signatures that many objects possess, and the highly refined vocalization and hearing structures of these species. By emitting ultrasonic pulses and analyzing the return signatures, bats can identify objects in the echoes and localize themselves within their surroundings. Of the approximately 1200 known species of bats, 85% use echolocation to navigate through the environment [1], and most of these species have specially adapted larynxes and other body parts that allow them to do this. Until recently, it was believed that bats lacking these structures could not echolocate, but in 2014 groundbreaking research was published showing that fruit bats, which were believed to be non-echolocating, produce bio-sonar clicks with their wings, resulting in a crude form of echolocation which can be used to detect and avoid collision with large surfaces [1].

A hallmark of almost all biological systems is the integration of robust neurological processing systems that assimilate and learn complex signatures such as those involved with echolocation. Within the last ten years we have seen a rapid maturation of machine learning (ML) approaches that are beginning to match the computational capabilities of biological systems for certain classification and prediction tasks. Though quite powerful, ML approaches often have certain limitations including the requirement for large training sets, inability to perform well in novel environments, and difficulty of justifying derived behaviors to establish trust in the operationalized artificial intelligence (AI) approach. To address these limitations, our colleagues at the Air Force Research Laboratory are developing a methodology to learn both the signature and meaning from the acoustic returns of a MAV using topological data analysis (TDA) [2].

Exploiting bio-inspired principles for optimized guidance and control (G&C) of aerial platforms has been an area of intense research for many years. Specifically, for micro air vehicles (MAVs), these research topics include studying and integrating principles of optic flow, mimicking biological olfaction systems for chemical sensing capabilities, and developing proprioceptive type sensors for autonomous flight stabilization. While these modalities have made significant gains within the MAV community, utilization of acoustic signatures for G&C has not been as widely explored. The focus of this effort is to exploit bio-inspired principles of acoustic localization, specifically using propulsion system generated noise, for improved situational awareness and G&C of MAVs.

MAVs may be instrumented with a variety of payloads including cameras and a host of other sensor systems. However, these platforms are limited by size, weight and power (SWaP) constraints, and each

additional sensor adds weight and consumes power, thereby reducing the effective flight time of the vehicle. Our approach is to draw inspiration from nature in utilizing the acoustic returns of emissions produced by MAV flight propulsion and control systems to recognize when the system is near an obstacle, such as a wall, ceiling, window, or open door. Small electrical motors are commonly used to power propellers on Group 1 UAS (e.g. blimps, quadcopters), and while self-generated noise from these motors is often considered an undesirable characteristic, we seek to develop approaches for exploiting vehicle self-noise to sense nearby objects and more effectively navigate through an environment. Some aspects of the self-noise can be tailored to our sensing application via choices of hardware components and electrical signals in the motor controller. The novelty of our approach is to use intrinsic self-noise without introducing an additional acoustic transducer to produce a source signal.

Small DC-powered motors/propeller systems for MAVs are complex acoustic noise sources with relatively few detailed studies possibly due to the diversity of the motor types available [3]. Besides the aerodynamic sound generated by the propellers, noise and vibration are generated due to electromagnetic, mechanical and electrical components. For example, acoustic noise is observed at the update frequency of the motor electronic speed controller (ESC) [4]. This was also observed in prior experiments conducted by our team on a quadrotor system with brushless motors. For a quadrotor, propulsion and control depend entirely on varying the speed of the propeller motors, requiring a wide range and fine control of RPM. For this reason, the rate at which the ESC updates the motor input is relatively high, with many standard quadrotor ESCs in the 8-24 kHz range.

In experiments with the quadrotor, we were interested in acoustic noise that could be exploited for both navigation and communications tasks. Our colleagues have utilized TDA to discern acoustic features that correlated with opening and closing a door, and we have analyzed update frequency modulation as a potential communication modality. The consistent and observable signal emitted at the update frequency provides a reliable basis on which to build a covert communications methodology for these systems. In the presence of changing vehicle maneuvers, flight conditions, and environments, an update frequency that can be independently modulated with negligible effect on flight performance provides possibilities for emitting user-defined acoustic signals that can be used to send messages to nearby cooperative vehicles and other co-combatants, or sensing the nearby acoustic environment.

In Section 2 results from our initial acoustic measurements from a variety of small motors are qualitatively and quantitatively described. In Section 3, we demonstrate several approaches for wall detection via the broadband interference structure of intrinsically generated noise from a small motor. In Appendix A an acoustic attenuation model is described which can be used to estimate the detectable range of the motor/propeller noise components as a function of frequency and the environment parameters (e.g. temperature and humidity). In Appendix B, the measurements taken during the first year of our project are tabulated and described.

2. FREE-FIELD MOTOR NOISE CHARACTERIZATION

We measure acoustic characteristics of brushed DC motors powered using an ESC-switched supply voltage, V_S . A pulse width modulation (PWM) control signal (defined by a switching frequency f_{pwm} and duty cycle d_{pwm}) is applied yielding an average supply voltage $d_{\text{pwm}}V_S$ to the motor. The PWM control signal is digitized at a sampling rate of 44.1 kHz on a Teensy microcontroller, and aliased frequency components of the control signal are also present in the voltage applied to the motor.

The motor/propeller systems produce a rich spectrum of acoustic noise consisting of contributions from mechanical components (motor bearings), electrical components (PWM update signals via ESC), electromagnetic components (brushes, armature and stator) and aeroacoustic noise (from propeller motion) [3]. We also note that the motor housing and mounting structure effect the noise and vibration through structural resonances that can vibro-acoustically couple into the emitted noise field. Figure 1 shows the 3D printed structural support and nearby microphones used in the motor measurements.

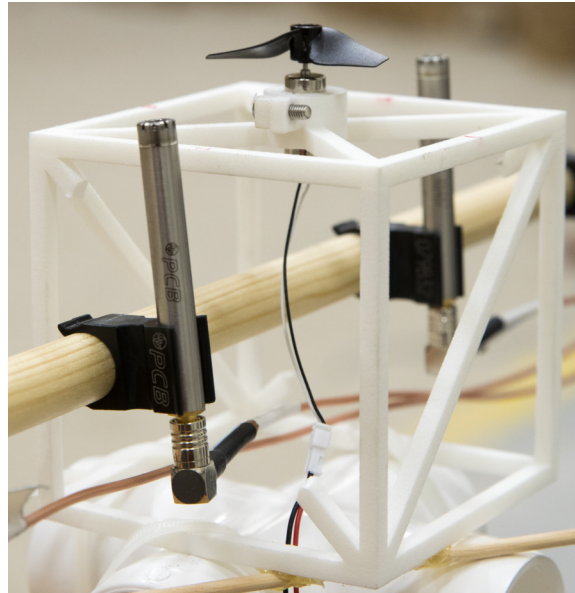


Fig. 1—Photo of motor in a 3D printed support structure, with nearby linear array of microphones.

Several combinations of small DC electric motors and propellers have been acoustically characterized in a static configuration (*i.e.* motor and microphones are mounted on a non-moving structure). The motors range in size between 4 and 8.5 mm and are powerful enough for small-model blimp propulsion and control. The measurements have been performed in several locations including inside a small anechoic chamber, and in various open lab areas without sound absorbing walls. This section summarizes the free-field acoustic measurement results (*i.e.* with no nearby reflecting wall present). The control signal sent to the motor ESC is generated using a Teensy microcontroller to allow user customized update frequencies and duty cycles. The goal of these measurements is to obtain a quantitative and qualitative understanding of the intrinsic motor noise over the update frequency, duty cycle parameter space for several motor and propeller types. A representative sample from the large measurement set is discussed in this section. Appendix B contains a listing of the measurements taken over the course of a year.

2.1 8 mm motor - June 14, 2019

Measurements of an 8 mm motor with 3-bladed propeller were taken in a laboratory room outside the anechoic chamber with the objective of characterizing the motor noise for several PWM signal types. The duty cycle for all of these tests is fixed at $d_{\text{pwm}} = 0.5$. Three types of PWM frequency f_{pwm} signals were considered: constant 5 kHz, periodic 5 sec up - 5 sec down linear ramp between 5 - 15 kHz; and periodic 1 sec up - 1 sec down linear ramp between 5 - 15 kHz. A four microphone linear array as shown in Figure 2

was set up on a laboratory bench with the wall removed. The microphones were recorded on Channels 0 - 3. In addition, three auxiliary data channels were recorded on Channels 4 - 6: motor power signal; piezo-electric sensor underneath motor frame; and PWM control signal. The propeller blade passage frequency (bpf) was measured with a hand-held digital photo laser tachometer to be approximately 46 kRPM (about 767 Hz).

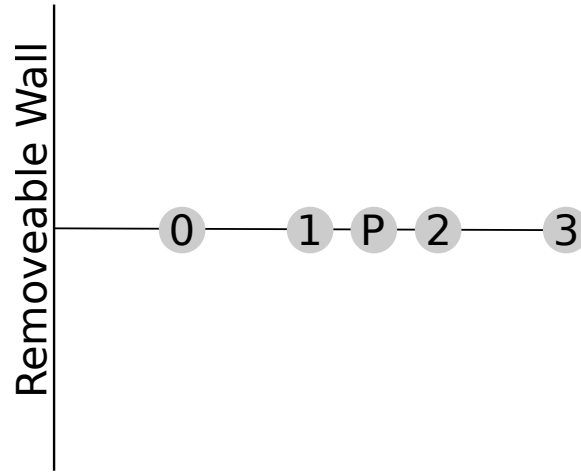


Fig. 2—Top view of linear microphone array measurement geometry and propeller. The microphones are equally spaced at 0.1 m, the motor/propeller system (P) is at the midpoint between Channels 1 and 2. Channel 0 is 0.105 m from the removable wall

Figures 3 - 4 show the acoustic power spectral density on microphone channel 0 for a constant PWM signal of $f_{\text{pwm}} = 5$ kHz, and duty cycle $d_{\text{pwm}} = 0.5$ over a 30 sec sample of data. The motor noise contains harmonic spectral lines spaced the motor rotation rate ($\text{bpf}/3 \sim 256$ Hz). As can be seen in Figure 4, the the motor rotation harmonics (numbers 18 - 22 are visible) vary over time, even for a constant PWM update frequency. Figure 5 shows time-averaged power spectra plots (split into multiple sub-band plots) for this same data for microphone channels 0 - 3 with harmonics of the motor rotation rate plotted as red vertical lines for reference. The third harmonic (corresponding to the blade passage frequency) is particularly strong. The acoustic spectral peaks correlate with the motor rotation rate harmonics especially in the 0 - 10 kHz band, although a noticeable broadening and shift of the peaks grows with increasing frequency.

Also visible in Figures 3 - 5 are frequency components related to the PWM control signal. From the magnified plot in Figure 4 it can be seen that there is a relatively strong and stable 5 kHz line at the PWM update frequency as well as weaker, stable (in frequency) spectral lines spaced at approximately 256 Hz from the 5 kHz line. The weaker spectral lines suggest a coupling between the motor rotation rate and the PWM control signal. Similar regularly space frequency components that track the PWM harmonics are observable PWM sweep measurements that we show below in Section 2.2. Harmonics of the PWM control signal are also visible in the noise spectrum. For example, a 5 kHz, 50 % duty cycle square wave will have harmonics at odd multiples of the fundamental frequency (*i. e.* 5, 15, ... kHz). PWM harmonics above the Nyquist sampling rate for the Teensy microcontoller (*i.e.* 22.05 kHz) will be aliased in the digitized PWM control signal, and thus be transmitted to the motor as we discuss below.

The spectral peaks associated with the PWM control signal tend to have narrower bandwidth than those associated motor rotation rate; this aids interpretation of the noise spectrum sources. In Figure 6 a comparison of the power spectra over the 0 - 22.05 kHz frequency band shows channel 0 (microphone signal) versus

channel 6 (PWM motor control signal) in the upper plot, channel 0 with the motor rotation harmonics in the middle plot, and a composite showing channels 0, 6 and the motor harmonics in the bottom plot. Although somewhat cluttered, these figures give some insight to the noise spectrum complexity. It should also be noted that the PWM control signal and ESC motor signals are not entirely clean; they contain spectral components in addition to those from a ideal square wave.

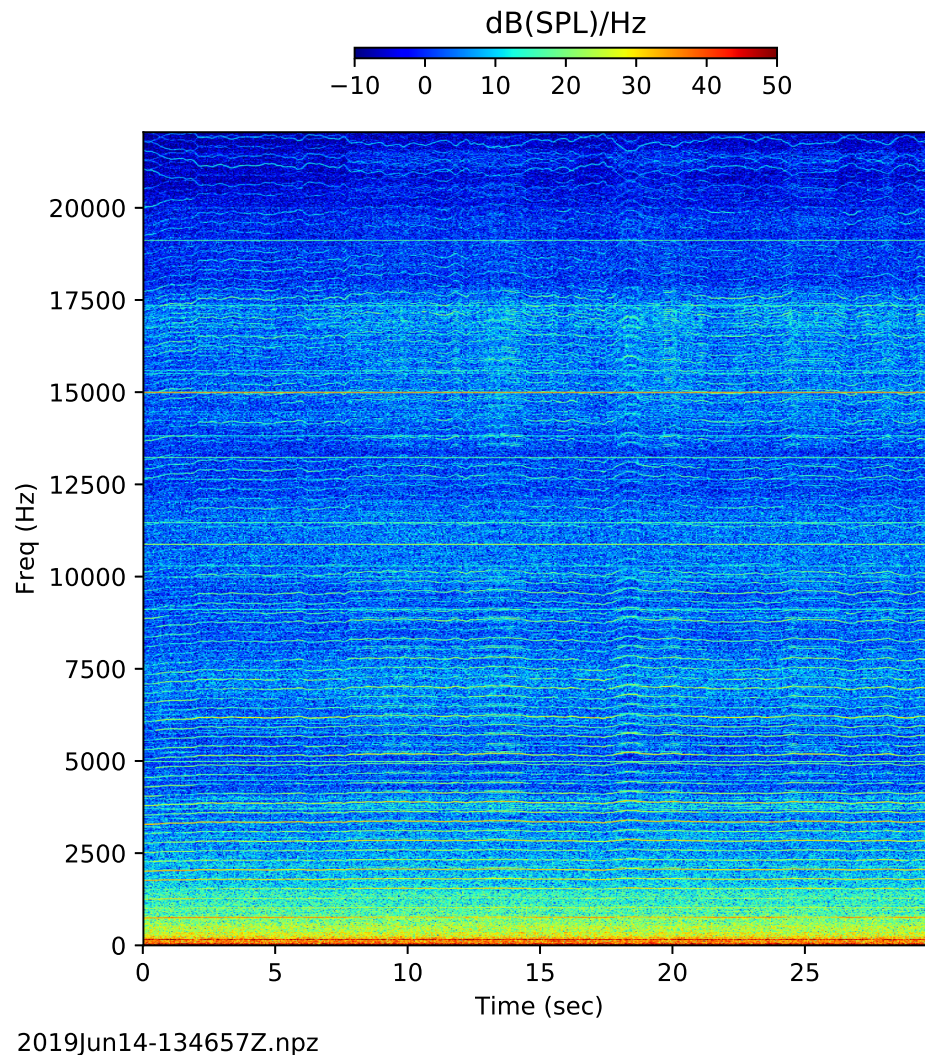
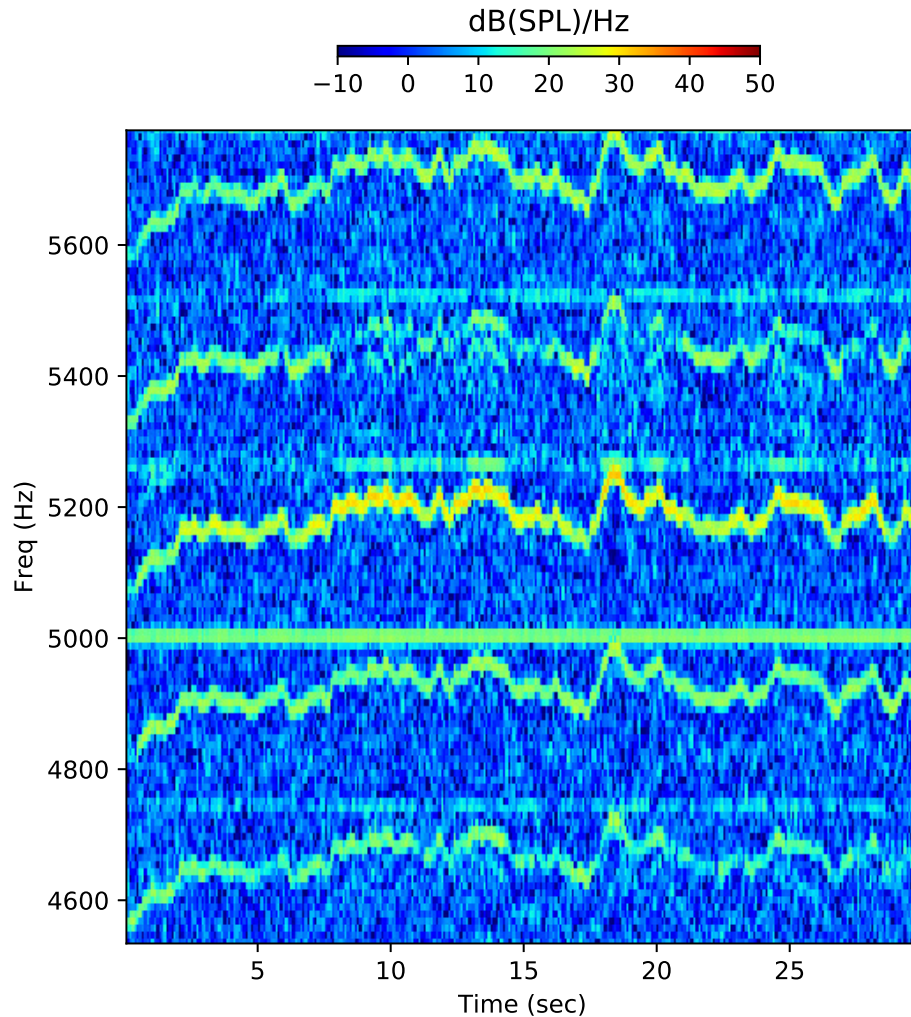


Fig. 3—Color plot of channel 0 power spectral density, dB(SPL)/Hz, taken in lab space outside of anechoic chamber for 8 mm motor with $d_{\text{pwm}} = 0.5$, $f_{\text{pwm}} = 5$ kHz, $n_{\text{fft}} = 4096$.

2.2 8.5 mm motor - February 28, 2019

An 8.5 mm motor with 3-bladed propeller was characterized inside a small anechoic chamber with the objective of measuring the motor noise at several different fixed d_{pwm} , f_{pwm} combinations, and for quasi-steady (*i.e.* slow) sweeps of the duty cycle or PWM update frequency while holding the non-sweeping parameter fixed. The power spectral density plots of the duty cycle sweeps are informative for discerning acoustic features that are correlated with changes in motor power for constant PWM frequency. The PWM frequency sweeps highlight the acoustic features that correlate with the PWM frequency for constant motor



2019Jun14-134657Z.npz, Channel 0

Fig. 4—Color plot of channel 0 power spectral density, dB(SPL)/Hz, taken in lab space outside of anechoic chamber for 8 mm motor with $d_{\text{pwm}} = 0.5$, $f_{\text{pwm}} = 5$ kHz, $\text{nfft} = 4096$. This plot is zoomed in to show the stability of the PWM frequency components compared to the blade harmonic frequency components.

power. The linear microphone array shown in Figure 2 was used in the anechoic chamber. No auxiliary channels were recorded.

Figure 7 is a spectrogram plot revealing a rich acoustic signature on Channel 0 as the PWM update frequency is linearly swept from 5 kHz to 15 kHz over approximately 8 minutes. The upward sloping PWM signal fundamental frequency as well as second and third harmonics are visible in the sweep. Also visible are the blade line harmonics (which are relatively constant due to the constant duty cycle, but do show variability as discussed in Section 2.1 above). Downward sloping spectral components associated with aliasing of the higher order PWM harmonics are also clearly visible. In addition, there are frequency components that run parallel to the PWM fundamental frequency component and with similar spacing to the motor rotation harmonics due to coupling between the motor rotation harmonics and PWM signal components.

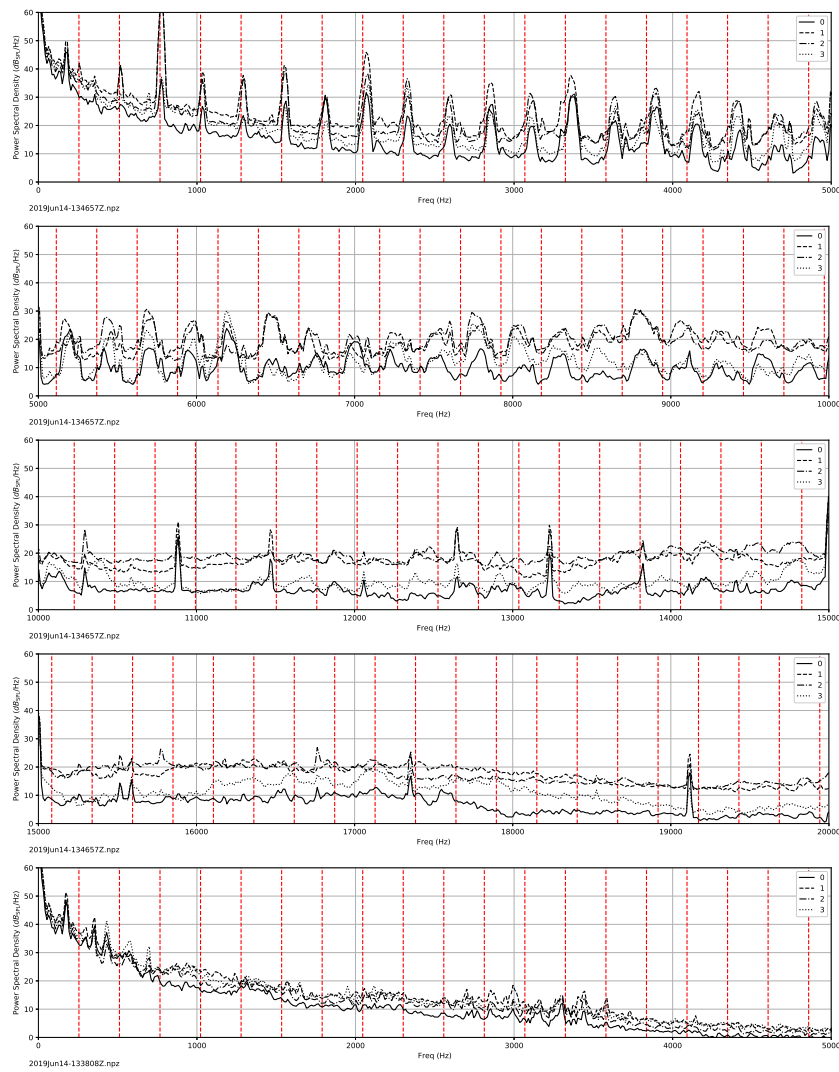


Fig. 5—Time-averaged (30 sec) channel 0 power spectral density ($\text{dB}_{\text{SPL}}/\text{Hz}$) with motor rotation rate harmonic frequencies plotted as red vertical lines, $n_{\text{fft}} = 4096$. (Top 4 plots) 8 mm motor, $d_{\text{pwm}} = 0.5$, $f_{\text{pwm}} = 5$ kHz. The power spectrum is split into 4 frequency bands to visualize the features: 0 - 5 kHz, 5 - 10 kHz, 10 - 15 kHz and 15 - 20 kHz; (Bottom) Ambient noise measurement power spectral density (averaged over 20 s) in the 0 - 5 kHz frequency band for comparison.

At approximately 301 s, the aliased frequency components cross at approximately 11.02 kHz. Potential advantages or disadvantage of operation at this PWM frequency will be the subject of future investigations.

Figure 8 is a spectrogram plot for a linearly swept duty cycle from 0.01 to 0.99 at constant PWM update frequency of 7 kHz. The constant frequency components related to the PWM signal are easily distinguishable from the motor rotation harmonics which increase with duty cycle. Between 20 % and 80 % duty cycles, the motor rotation harmonics are approximately linearly related to the duty cycle. The adjustment of the motor speed is also visible during discrete stepping of the duty cycle. The broadband noise components increase with duty cycle, but the rate of increase is frequency dependent.

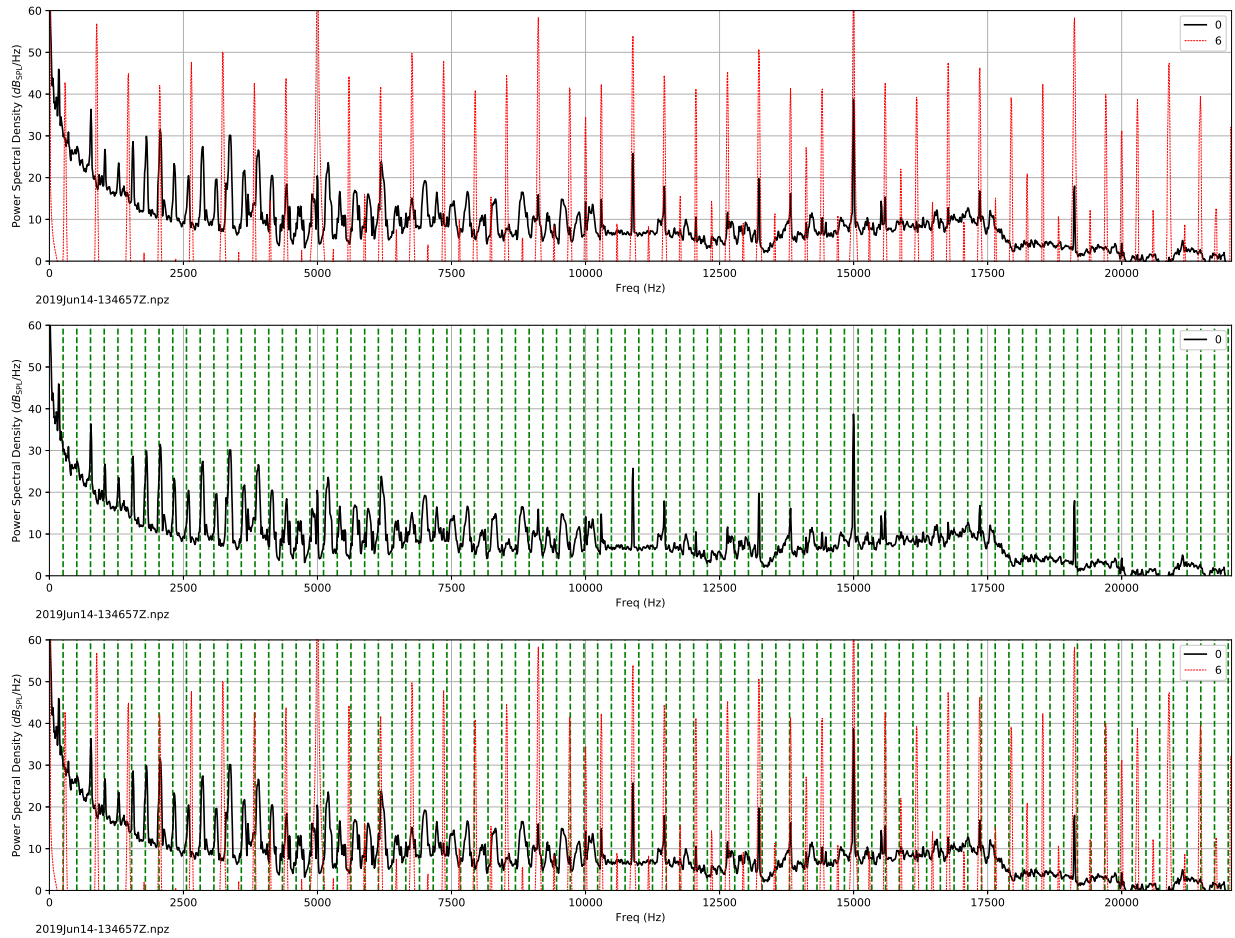


Fig. 6—Power spectral density plots comparing the microphone, scaled PWM signal, and motor rotation harmonics over the 0 - 22 kHz frequency band for the 8 mm motor with $d_{\text{pwm}} = 0.5$; $f_{\text{pwm}} = 5$ kHz, $n_{\text{fft}} = 4096$. (Top) Channel 0 (microphone, black) and channel 6 (scaled PWM control signal, red) (Middle) Channel 0 (black) with motor rotation rate harmonics (green), (Bottom) a composite plot showing microphone (black), PWM signal (red), and motor rotation harmonics (green)

2.3 8 mm motor - August, 15 2019

In this section, we describe measurements of an 8 mm motor with 3-bladed propeller taken in the LASR desert high bay with the objective of assessing the directionality of the motor noise. The motor/propeller is mounted at the center of a 6-channel circular microphone array as shown in Figure 9. The microphones are equally spaced (60 degree spacing) along the circumference of the array and approximately 0.258 m from the motor center. Two minute segments of motor-on and motor-off (ambient) were taken for two different trials as summarized in Table B21. The microphone channels were moved by 60 degrees between the two trials.

Figures 10 and 11 show inter-station (stations are fixed locations with respect to the propeller) and inter-channel (channels are microphones labels) power spectral density measurements and their differences between the two motor noise measurement trials. The inter-channel differences (at a fixed station) are generally smaller than the inter-station differences (for a fixed channel) indicating a frequency-dependent

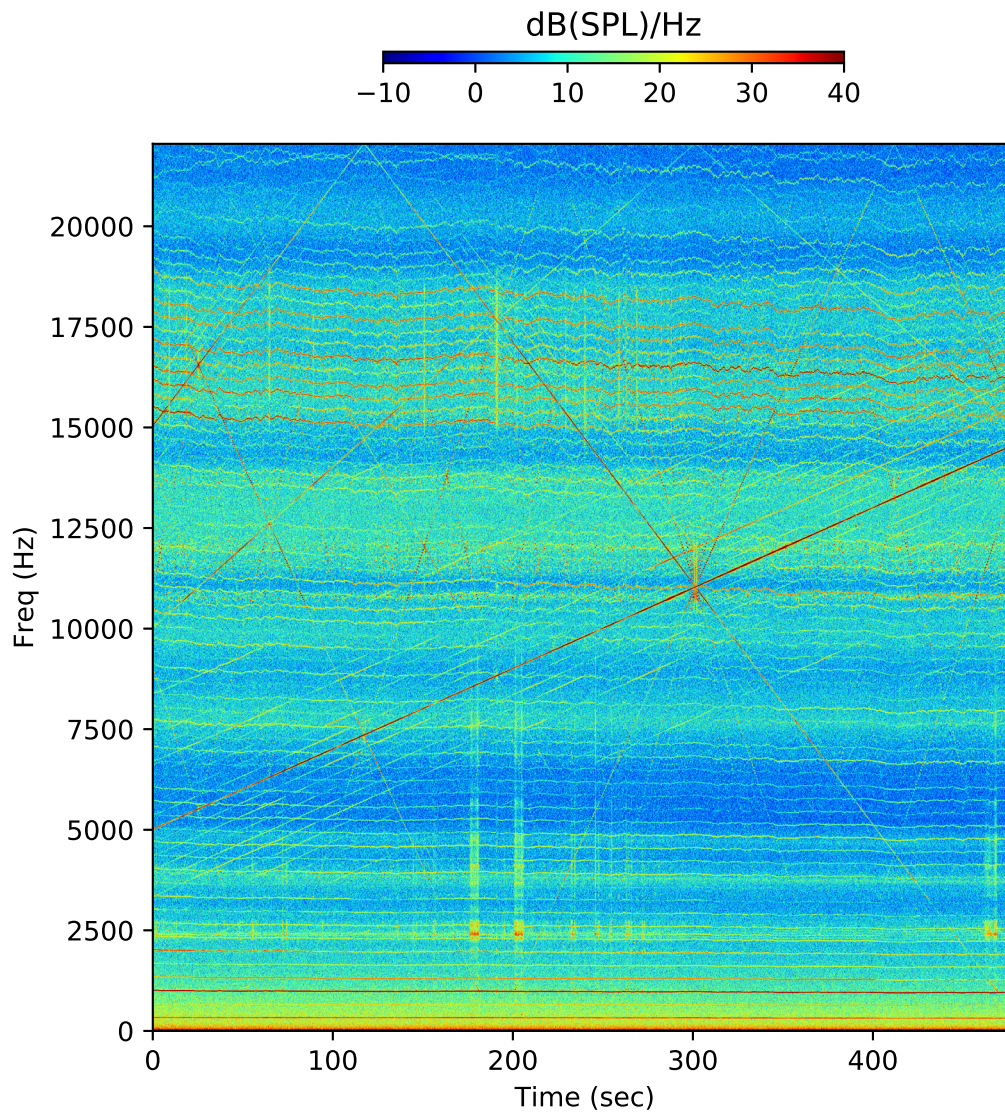


Fig. 7—Color plot of channel 0 power spectral density for PWM linear frequency sweep from 5 - 15 kHz for 8.5 mm motor at constant duty cycle, $d_{\text{pwm}} = 0.5$, and $n_{\text{fft}} = 4096$.

directionality in the motor noise amplitude. Figures 12 and 13 show inter-station and inter-channel power spectral density measurements and their differences between the two ambient noise measurement trials. The inter-channel differences are generally comparable to the inter-station differences indicating that the ambient noise is similar at the array stations.

3. MOTOR SELF-NOISE IN THE PRESENCE OF A REFLECTING WALL

In this section, we consider modifications of the motor self-noise field induced by the presence of a reflecting wall and derive signal processing approaches for inferring the wall distance from measurements of the acoustic field. We begin by analyzing a simplified geometry with a microphone between a noise

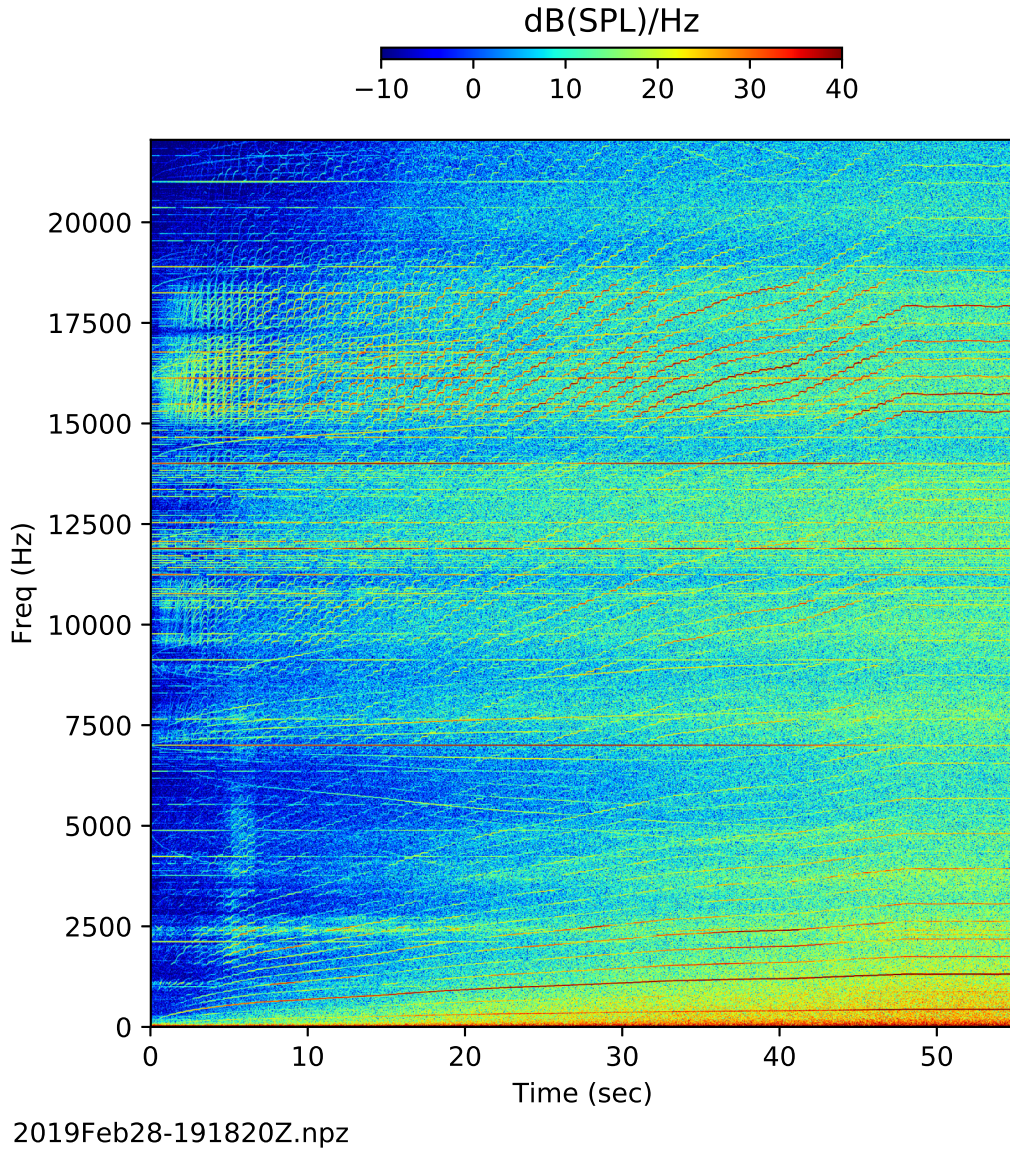


Fig. 8—Color plot of channel 0 power spectral density for duty cycle sweep from 0.01 - 0.99 for 8.5 mm motor at constant PWM frequency $f_{\text{pwm}} = 7\text{kHz}$, and $\text{nfft} = 4096$.

source (a motor/propeller system in this case) and a plane reflecting wall. Figure 14 shows a schematic 2D representation with the acoustic source and receiver located at the foci of an ellipse given by

$$\frac{x^2}{a^2} + \frac{y^2}{b^2} = 1, \quad a = d + \Delta d, \quad b = \sqrt{\Delta d(2d + \Delta d)}.$$

where a, b are the ellipse semi-major and semi-minor axes respectively, $2d$ is the source to receiver separation, and $2\Delta d$ is a parameter defining the path length difference between the direct (SR) and reflected (SPR) paths. Note that the normal to the ellipse at P bisects the angle $\angle SPR$, thus the path satisfies the law of reflection for a flat wall tangent to the ellipse. The ellipse is the locus of points with equal total path length

between the source and the microphone, thus for a constant sound speed, an acoustic wave traveling along a reflected path from any point on the ellipse will have the same delay time relative to the direct path between the source and microphone. The phase difference between the direct and reflected waves will vary with the acoustic wavelength, thus the microphone will potentially measure a frequency-dependent interference pattern that is convolved with a broadband acoustic source spectrum. Here we investigate the feasibility of sensing the presence of a nearby acoustic reflector via the interference between the direct and reflected paths.

In our case, the acoustic source spectrum of a motor/propeller system is broadband, and directional. The phase coherence between different azimuthal orientations from the motor will impact whether or not an interference between direct and reflected paths is observed. We will first investigate the geometry with the wall normal to the line connecting the source and receiver so that the azimuthal direction from the source is identical for both paths. Additionally the wall acoustic reflective properties will modify the reflected wave. Approaches for processing single and multiple microphone channels via cross-correlation are described in this section and tested with data collected from statically mounted motor/propeller systems in the vicinity of a wall.

3.1 Model for a broadband interference pattern

The frequency content of the motor/propeller systems is broadband over the audible range with peaks related to the motor, ESC refresh rate, and aeroacoustic noise due to the propeller. In the frequency domain, we model the received pressure at the microphone $\hat{p}_m(\omega)$ as the sum of direct $\hat{p}_d(\omega)$ and reflected waves,

$$\hat{p}_m(\omega) = \hat{p}_d(\omega) + a_r \hat{p}_d(\omega) e^{-i\omega\tau} \quad (1)$$

where the complex coefficient a_r incorporates spreading, and reflection losses as well as a phase shift ϕ , and the exponential term is a time delay $\tau = 2\Delta d/c$ relative to the direct arrival, where c is the sound speed. The power spectrum at the microphone is the product of the direct-wave power spectrum and an oscillatory interference term,

$$|\hat{p}_m|^2 = |\hat{p}_d|^2 \left(1 + |a_r|^2 + 2|a_r| \cos(\omega\tau - \phi) \right),$$

which yields the following frequency separation between the interference maxima

$$\Delta f = 1/\tau = c/(2\Delta d), \quad (2)$$

where $2\Delta d$ is the path length difference between the directed and reflected arrivals.

Figure 15 is a plot of interference term for an idealized rigid wall and assuming spherical spreading from a point source $a_r = 1/(1 + \Delta d/d)$ with $d = 0.075$ m, and $\Delta d = 0.1$ m. The interference term is convolved with the non-white source spectrum from the motor/propeller system, making it difficult to discern the interference pattern from the intrinsic complexity of the motor/propeller system free-field noise power spectrum in the raw data. If it is known, the free-field power spectrum can be used to normalize the microphone power spectrum. This approach is demonstrated in Section 3.2 using a single microphone. In practice, the motor propeller system is a non-stationary noise source with significant variability based on the operational state of the MAV so we propose we propose multi-channel cross-correlation as another method to remove the source spectrum in Section 3.3.

3.2 Example with a known free-field source power spectrum

In this section, we compare noise measurements from a statically mounted motor/propeller system in the presence of a nearby plywood wall with measurements without the wall. Initially, we consider a geometry with the motor and microphone oriented as shown in Figure 2. For this case, the direct and reflected acoustic paths overlap between the motor and the microphone, and the path length difference, $2\Delta d$, is the perpendicular distance from the microphone to the wall. Note also that for this geometry the direct and reflected paths are ensonified by noise field emitted from a single source azimuth (*i.e.* the phase is coherent); for other wall geometries tangent to the ellipse, the direct and reflected paths will be sampling noise emitted from two different azimuthal directions.

3.2.1 8 mm motor - June 14, 2019

Acoustic measurements of noise from an 8 mm DC electric motor with 3-bladed propeller were made with a several microphones in the vicinity of a plywood wall, and repeated with the wall removed. The propeller blade passage rate was measured to be approximately 46000 rpm (767 Hz) which corresponds to a motor rotation rate of approximately 256 rotations per second. Figure 2 shows the experimental setup with the wall in place; the four microphones were uniformly spaced at 0.1 m and the distance from microphone channel 0 to the plywood wall was approximately 0.105 m. In Figure 16, the upper left plot shows the noise power spectral density (PSD) (Channel 0, averaged over 30 sec) comparison for the wall present and removed, as well as the ambient noise level (Channel 0, averaged over 20 sec) taken at a later time (nfft = 256). For this data, the parameters of the PWM motor control signal are $f_{\text{pwm}} = 5000$ Hz, $d_{\text{pwm}} = 0.5$. The bottom left curve in Figure 16 is the difference between the wall present and wall removed power spectral densities for Channel 0 which reveals a noisy oscillatory modulation with respect to frequency that is particularly apparent between 10 - 20 kHz with approximate spacing between the interference maxima 1600 Hz. The interference pattern is related to the time delay, τ , between the direct and reflected paths as shown in the analysis in Section 3.1. The Fourier transform of the dB difference is shown in right plot of Figure 16 and clearly shows a peak at this oscillation period $6.31\text{e-}4$ s corresponding to 1560 Hz.

3.2.2 8 mm motor - Aug 14, 2019

An 8-channel linear microphone array with element spacing 0.02 m was placed between a removable wall and a statically mounted 8 mm motor/propeller system as shown in Figure 17. Figure 18 shows the difference between power spectral density measurements for the wall/no-wall cases. An interference pattern with period depending on the microphone to wall spacing is discernible from these plots for Channels 0 - 5 (the channels are numbered left to right with Channel 0 is closest to the wall). Figure 19 shows the spectral content of the dB difference curves with x-axis corresponding to the time delay difference between the direct and reflected arrivals. The dashed vertical lines correspond to the expected arrival times based on the wall spacing from Channel 0 of 0.0173 m (left plot) and 0.117 m (right plot). In the right plot, the interference peak for Channel 4 (0.197 m from wall) is still discernible but approaching the noise level of the plot.

3.3 Cross-correlation processing

In the preceding section, we applied a measurement of the no-wall (free-field) acoustic power spectrum to normalize the near-wall acoustic measurement which revealed the broadband interference structure between the direct and reflected paths. Another approach for wall detection and localization utilizes cross-correlation of microphone channels and is described in this section. This technique does not require

a free-field measurement, but uses the signal on at-least two microphone channels to form a generalized cross-correlation (GCC). The cross-correlation contains time-delay information which can be extracted via GCC techniques to estimate the round-trip travel time to the wall [5]. It is important to point out that simple cross-correlation (without the spectral whitening of GCC approach) or autocorrelation of a single channel does not reveal arrival structure because the correlations are dominated by the strong spectral peaks of the motor power spectrum. The GCC approach normalizes (whitens) the pressure snapshots before cross correlation to overcome the strong amplitude spectral peaks while preserving the phase of the microphone signals.

The cross spectral density matrix is estimated by,

$$C_{ij}(\omega) = \langle \tilde{p}_i \tilde{p}_j^* \rangle \approx \frac{1}{N_s} \sum_{k=1}^{N_s} \tilde{p}_i^k(\omega) \tilde{p}_j^{k*}(\omega) \quad (3)$$

where $\tilde{p}_i^k(\omega)$ is the normalized complex pressure on array channel i at time index k , $*$ denotes complex conjugation and $\langle \dots \rangle$ the expected value which is approximated by a sum over N_s array snapshots. A snapshot is a short-time FFT of the acoustic pressure on a given channel. The normalized pressure is given by

$$\tilde{p}_i = \frac{\hat{p}_i}{|\hat{p}_i|}. \quad (4)$$

The generalized cross correlation (GCC) for a microphone pair is inverse Fourier transform of $C_{01}(\omega)$, the off-diagonal term of the cross spectral density. Figure 20 shows the GCC result for data measured on August 14, 2019 without a wall (top), and with a wall present at 0.117 m from the closest microphone (bottom). The seven line plots correspond to the GCC between Channel 0 and the other seven array microphones. The top plot shows distinct peaks associated with the direct path arrivals for Channels 1 - 6; the peak for Channel 7 is degraded in comparison because it is closest the flow turbulent generated by the propeller. In the lower plot with the wall present, in addition to the peaks associated with the direct path arrivals, weaker time-delay peaks associated with wall reflection are observed. The cross correlations for this example are 10 snapshots of 4096 sample data segments with 50% overlap (approximately 0.5 seconds of data).

For reflecting wall positions comparable to the direct path distance from the propeller, the weaker reflected arrivals in the GCC will overlap with the stronger direct path arrivals. One approach for filtering out the direct path contribution (to emphasize the reflected path) is to define a modified two-microphone cross-correlation processor from the elements of a 2×2 cross-spectral density matrix as,

$$X_{01}(\omega) = e^{i\omega\delta/c} C_{01} - e^{-i\omega\delta/c} C_{10} \quad (5)$$

where ω is circular frequency, c is the sound speed, and δ is the spacing between the channels. The peaks in the inverse FFT of X_{01} correspond to round-trip acoustic travel time between Channels 0, 1 and the wall.

Figure 21 shows an application of the generalized cross-processor to the same August 14, 2019 data set that was processed in Section 3.2.2 with the single microphone approach. Array channels 0, 1 (microphone channel 0 is the closest to the wall) are used to form X_{01} using Equation 5. For this example, the channel spacing is $\delta = 0.02$ m, we assume a sound speed of $c = 343$ m/s, the snapshot length (*i.e.* nfft) is 2048

with 50 percent overlap, and we use 4 snapshots (about 0.1 sec of data) to estimate the cross spectral density matrices. The four frames correspond to different distances between Channel 0 and the wall which are 0.017 m, 0.066 m, and 0.117 m, and no wall for the upper left, upper right, lower left and lower right frames respectively. For each frame the upper plot is an average of the cross-correlations for the entire data set (over 1.5 minutes) with the actual Channel 0, 1 time-delays (computed in the lab from a distance measurement) shown as dashed vertical lines, and the lower color figure shows a stacking of the cross-correlations over 0.1 second intervals. This example shows that the cross-correlation approach can recover the reflection delays using 0.1 second segments of data.

Another related approach for estimating the wall distance is formulated by comparing the measured cross spectral density estimate with a modeled pressure parameterized by τ_j , the relative time delay between the direct and reflected arrivals,

$$J(\boldsymbol{\tau}; \boldsymbol{\omega}) = \sum_{i,j} \tilde{r}_i^* C_{ij} \tilde{r}_j \quad (6)$$

where \tilde{r}_i is the modeled complex pressure at microphone i , and is developed below. The cross-spectral density and model pressure are normalized so the energy function given by $E = 1 - J(\boldsymbol{\tau}; \boldsymbol{\omega})$ is zero for a perfect match between the measured data and modeled replica pressure.

Our model for the acoustic pressure at a microphone is given by Equation 1 with the direct wave modeled as a point source,

$$\hat{p}_j^d(\boldsymbol{\omega}) = S(\boldsymbol{\omega}) G_j^d(\boldsymbol{\omega}) = S(\boldsymbol{\omega}) \frac{e^{-i\boldsymbol{\omega}\tau_j^d}}{2d_j} \quad (7)$$

where τ_j^d is the direct path (*i.e.* propeller to microphone) travel time, $S(\boldsymbol{\omega})$ is the source spectrum, and $2d_j = c\tau_j^d$, and G_j^d is the point source free-field Green's function. Substituting Eq. 7 for \hat{p}_k^d yields,

$$\hat{r}_j = S G_j^d (1 + a_j e^{-i\boldsymbol{\omega}\tau_j}) = S G_j^d H_j \quad (8)$$

where the notation $H_j = 1 + a_j e^{-i\boldsymbol{\omega}\tau_j}$ is introduced for the transfer function. The normalized array modeled pressure vector is,

$$\tilde{r}_j = \frac{S}{|S|} \frac{G_j^d H_j}{|G_j^d H_j|} \quad (9)$$

From Eq. 9 it can be seen that the modeled pressure depends upon the unknown time delays τ_j and the wall reflection coefficient and is independent of the source spectral amplitude. The unknown source phase $S/|S|$ drops out from the form of the cost function, Eq. 6.

Figure 22 shows the results from applying this to the August 14, 2019 acoustic data. Channels 0, 1 (two channels closest to wall) of the linear array were used to estimate the Channel 0 to wall distance with the optimization given in Equation 6. The plots show the optimization for the Channel 0 to wall distance at the minimum of an energy functional defined $E = 1 - J$. Four different cases were measured: corresponding to Channel 0 distances to the reflecting wall of 0.017, 0.066, 0.117 m, and two trials with the wall removed. The red dashed vertical line in the top three plots shows the actual Ch 0 to wall distances, and the bottom

two are for the no wall test cases. A minimum in the cost function occurs near the measured value with a bias that increases with increasing distance from the wall.

4. CONCLUSIONS

We have presented an experimental setup, results, and analysis for characterizing the acoustic signatures of propulsion system components representative of those on micro air vehicles. Analyzing data from multiple motors and motor operating conditions, and with different microphone array configurations, we have identified features in the acoustic signatures that can be exploited for localization and navigation tasks. These features include frequencies associated with motor update rate and duty cycle, as well as interference patterns that result from the presence of near-field reflective objects. We have demonstrated that acoustic interference patterns can be used to detect and compute a relative distance to a wall surface using a single microphone channel. Cross-correlation processing methods for two microphone channels has also been demonstrated to estimate the distance to a nearby wall.

Following on this work, we are developing algorithms for relative wall position control using real-time feedback of acoustic data produced from the motor propeller system, and investigating machine learning techniques for more advanced on-board processing of acoustic data. We are beginning measurements to demonstrate the feasibility of extracting the broadband interference pattern using motor self-noise on moving platforms, and understand the effect of motor self-noise directionality on distance limits and geometries for wall detection/distance estimation. We have identified noise components from the PWM control signal, and in future work will investigate the potential of using strong narrowband noise components to extend the range of object detection, and potentially measure and utilize ultrasonic components of the motor noise. Other areas of continued work will involve optimizing microphone geometries for environmental sensing and communications and developing a better understanding of the noise source components and their coupling. PWM chirps and sweeps will also be further investigated for applications to sensing nearby objects and communications.

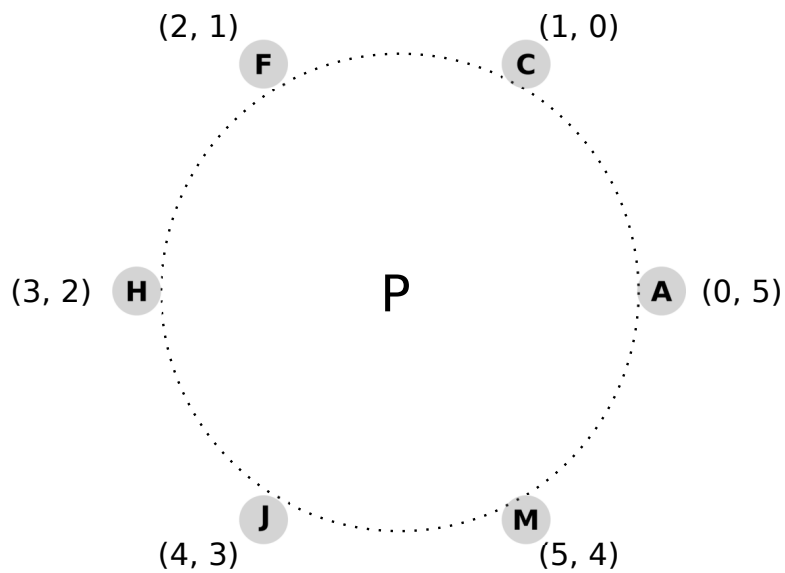


Fig. 9—(Top) Photo of 6-channel circular microphone array with equally spaced microphones (60 degree spacing) and 0.258 m from motor center. (Bottom) Diagram (top view) of circular array geometry with array stations labeled (fixed with respect to the propeller). The array channels for the two trials are indicated in parentheses for the first and second trials.

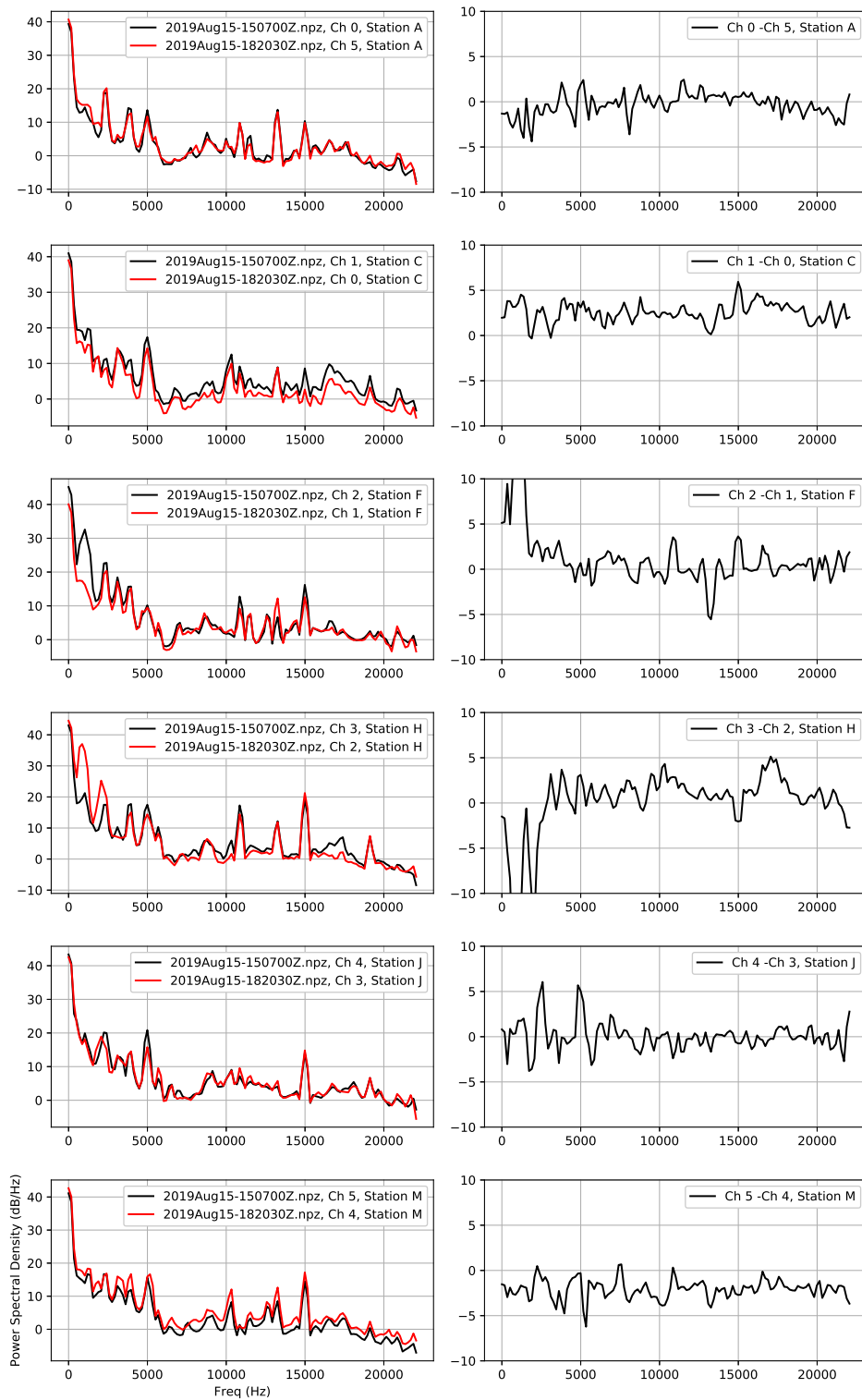


Fig. 10—Comparison of power spectral density measured at a given station (stations are fixed microphone locations relative to the motor) for two measurement trials. The microphone channels were rotated by 60 degrees between the trials. Left column shows the power spectral density for the two trials (nfft = 256, averaged over 2 minutes), and the right column shows the difference (in dB) between the two curves. This plot shows that the inter-channel differences between the two motor noise trials for a fixed station.

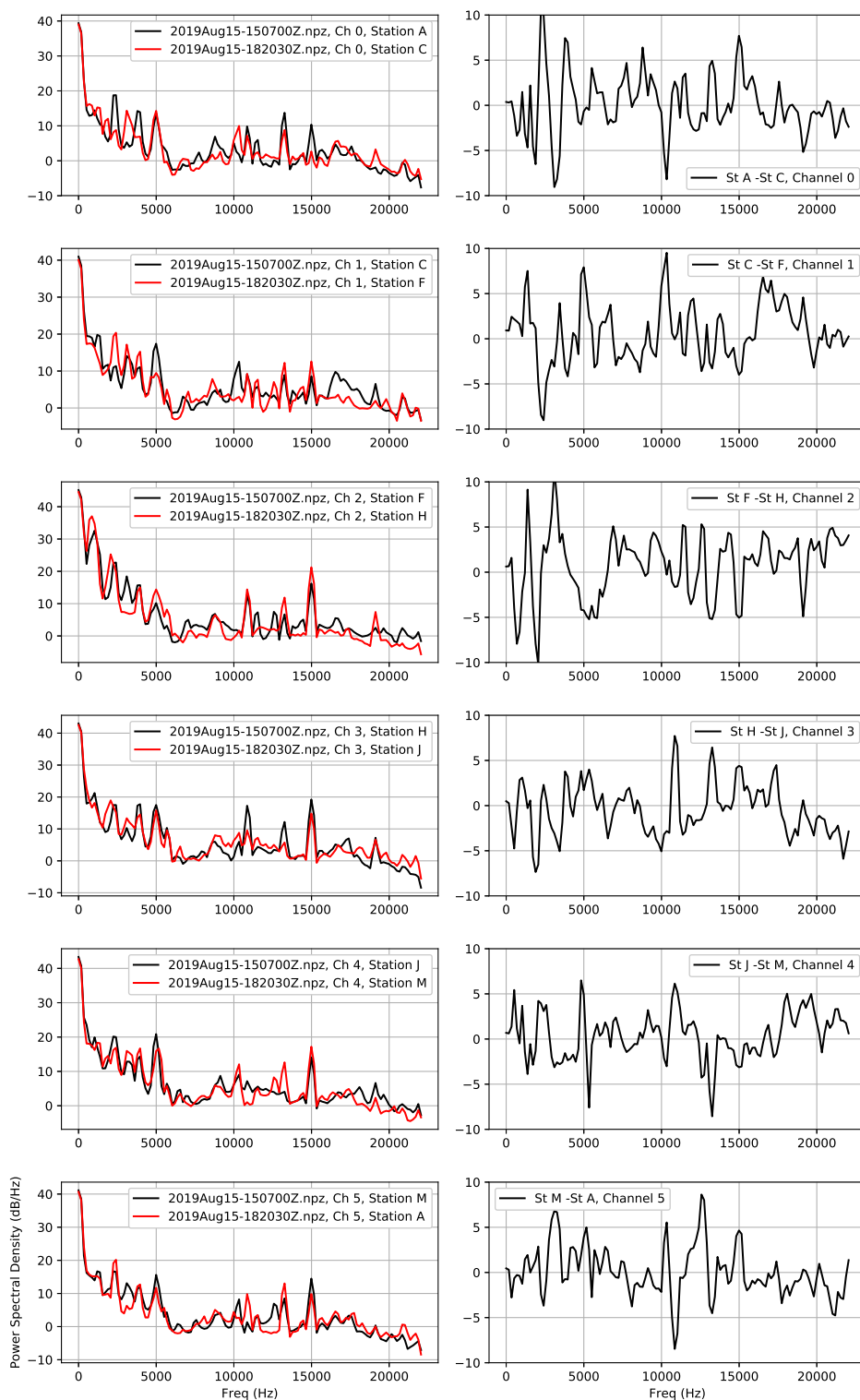


Fig. 11—Comparison of power spectral density measured on a given microphone channel for two measurement trials. The microphone channels were rotated by 60 degrees between the trials. Left column shows the power spectral density for the two trials (nfft = 256, averaged over 2 minutes), and the right column shows the difference (in dB) between the two curves. This plot shows that the inter-station differences between the two motor noise trials for a fixed microphone channel.

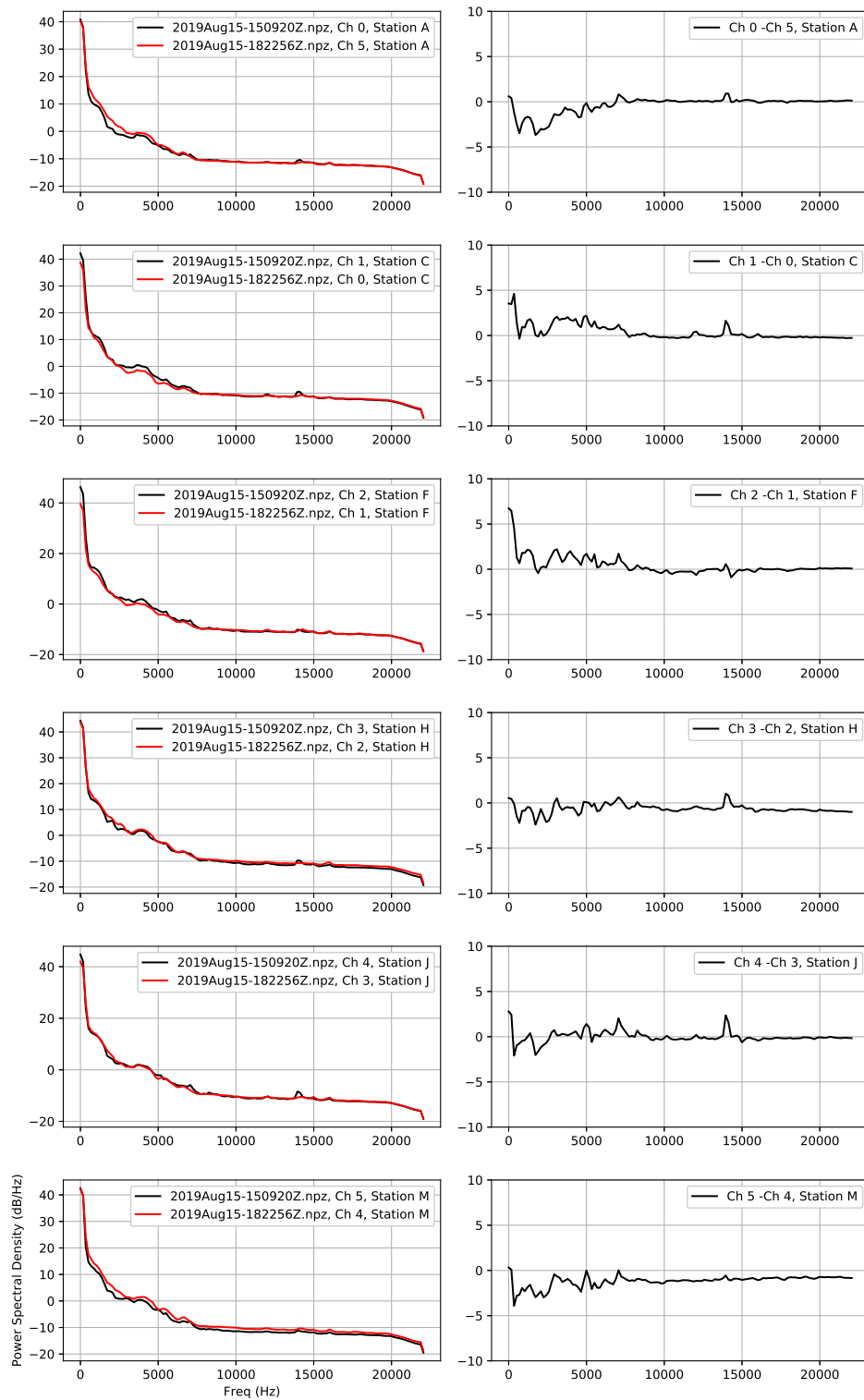


Fig. 12—Comparison of power spectral density measured at a given station (stations are fixed microphone locations relative to the motor) for two measurement trials. The microphone channels were rotated by 60 degrees between the trials. Left column shows the power spectral density for the two trials (nfft = 256, averaged over 2 minutes), and the right column shows the difference (in dB) between the two curves. This plot shows that the inter-channel differences between the two ambient noise trials for a fixed station.

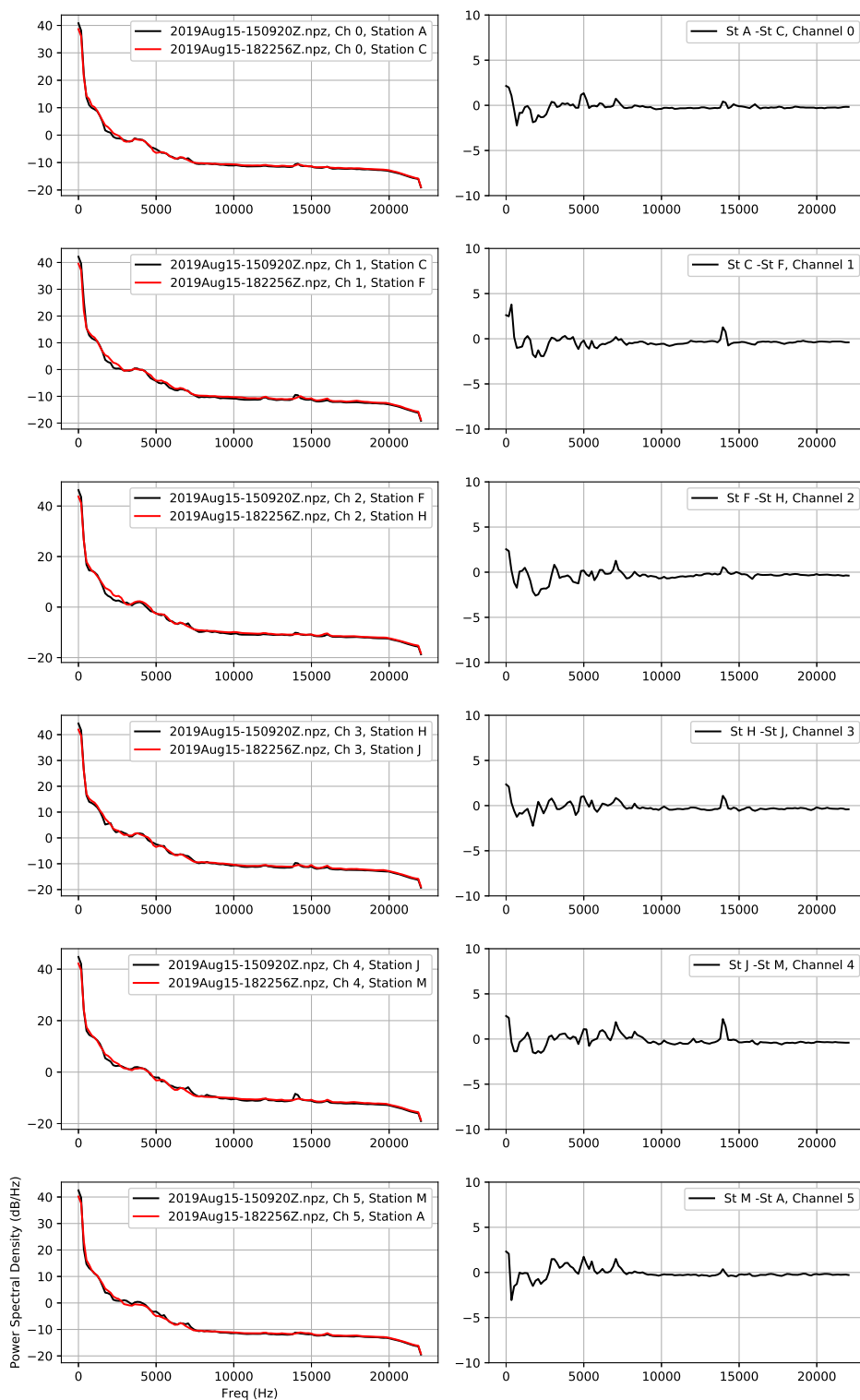


Fig. 13—Comparison of power spectral density measured on a given microphone channel for two measurement trials. The microphone channels were rotated by 60 degrees between the trials. Left column shows the power spectral density for the two trials (nfft = 256, averaged over 2 minutes), and the right column shows the difference (in dB) between the two curves. This plot shows that the inter-station differences between the two ambient noise trials for a fixed microphone channel.

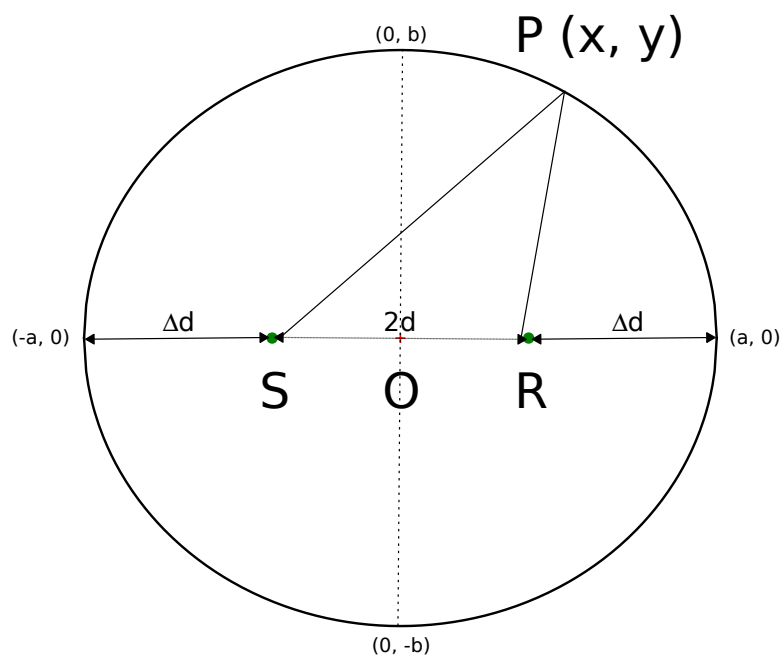


Fig. 14—2D geometry showing acoustic source (motor) S , receiver (microphone) R , with separation $2d$ placed at the foci of an ellipse. The difference between the direct ray path (SR) and the reflected ray path (SPR) is $2\Delta d$ for all points on the ellipse.

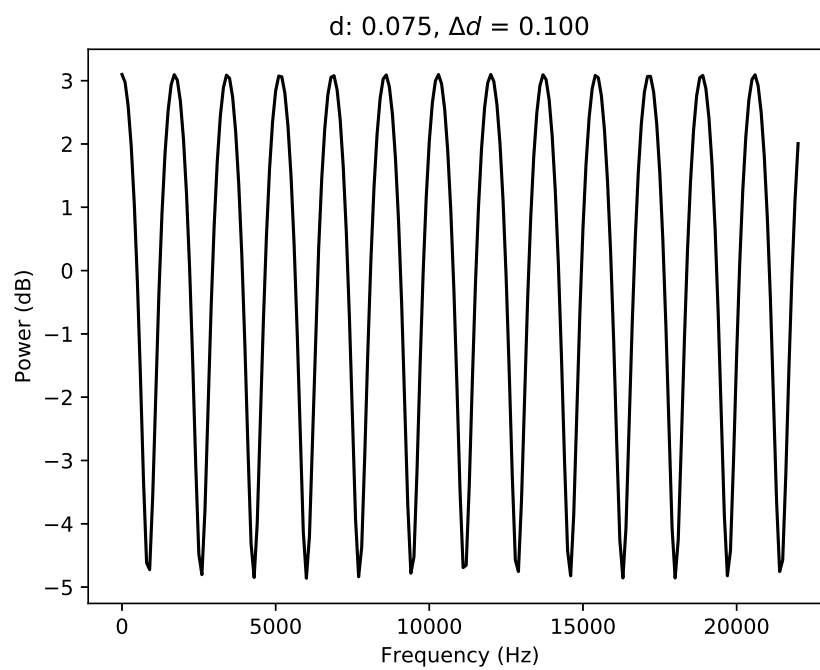


Fig. 15—Amplitude (dB) of interference term due to reflection from a rigid wall with $d = 0.075$ m, and $\Delta d = 0.1$ m

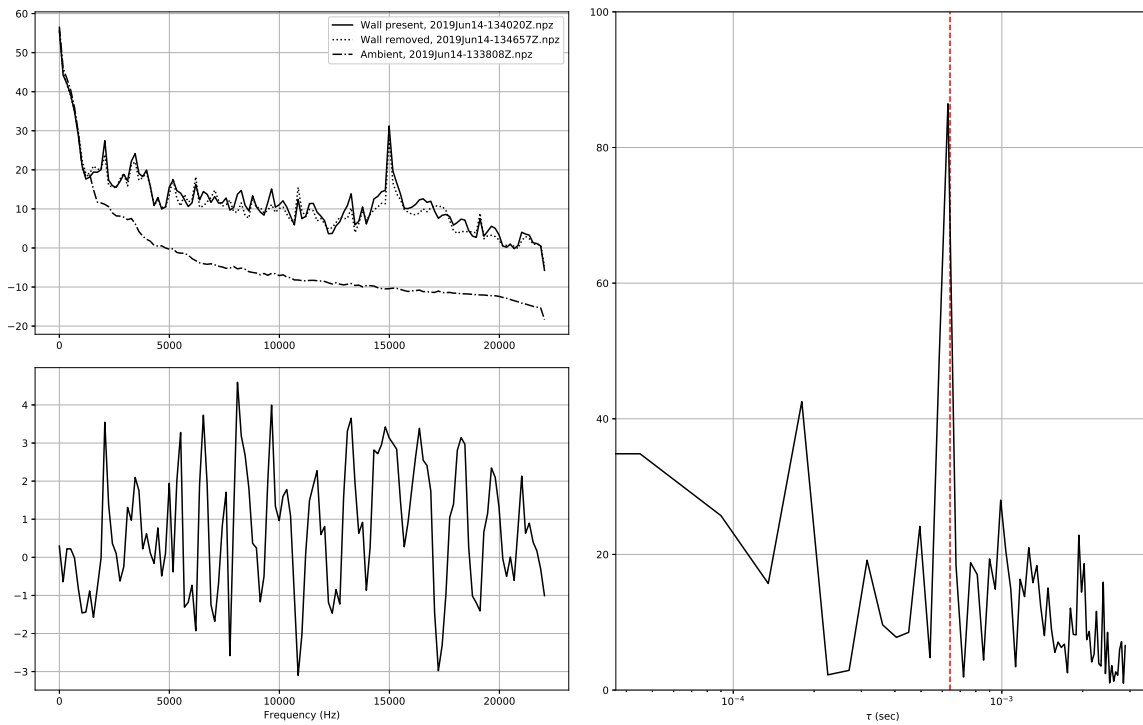


Fig. 16—(Top Left) Power spectral density plot of Microphone 0 with wall present (averaged over 30 s), wall removed (averaged over 30 s), lab ambient (averaged over 20 s) computed with $nfft = 256$. (Bottom Left) Power spectral density dB difference between wall present and wall removed curves shown in upper left. (Right) Spectral content of dB difference curve (shown in lower left) computed with an FFT. The x-axis corresponds to the round-trip delay time of the reflected path relative to the direct path. The red vertical line shows the expected peak location from Equation (2) with $c = 343$ m/s and $\Delta d = 0.11$ m.

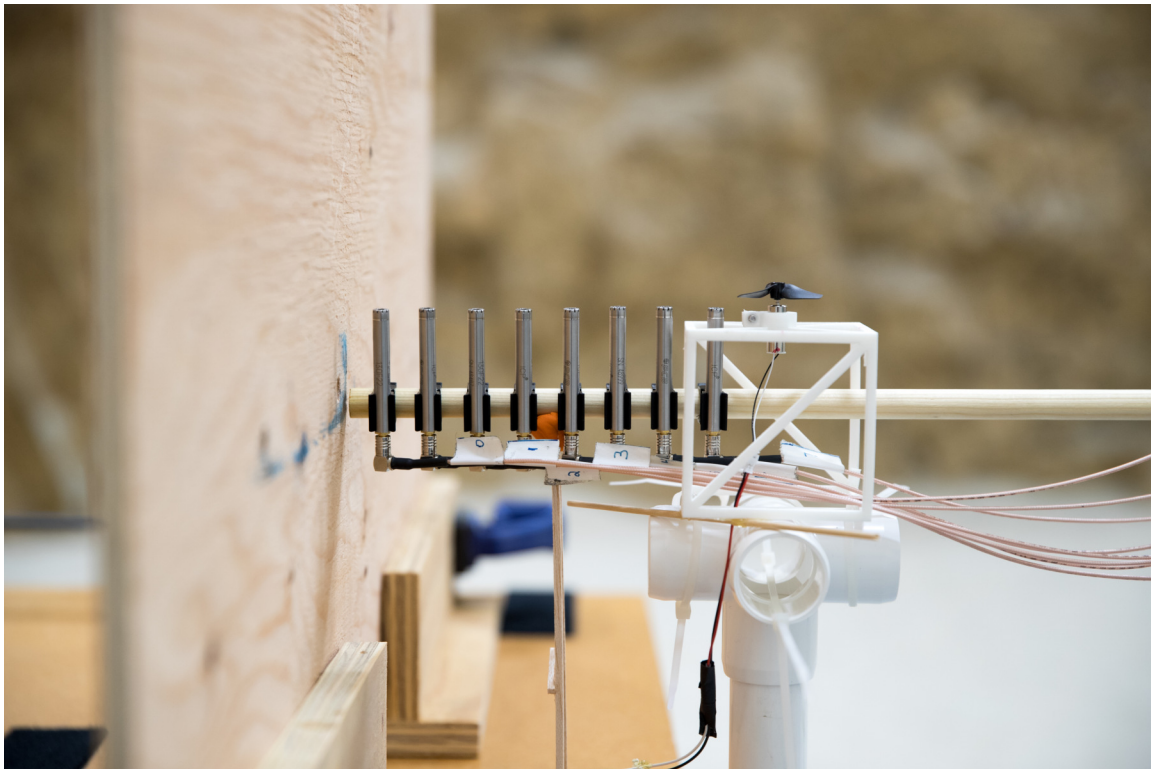


Fig. 17—Photo of 8-channel linear microphone array between a removable wall and mounted 8 mm motor/propeller system. The distance from the wall to Channel 0 (the closest microphone to the wall) is 0.015 m, the microphone spacing is 0.02 m, and the distance from Channel 7 to the propeller is 0.026 m.

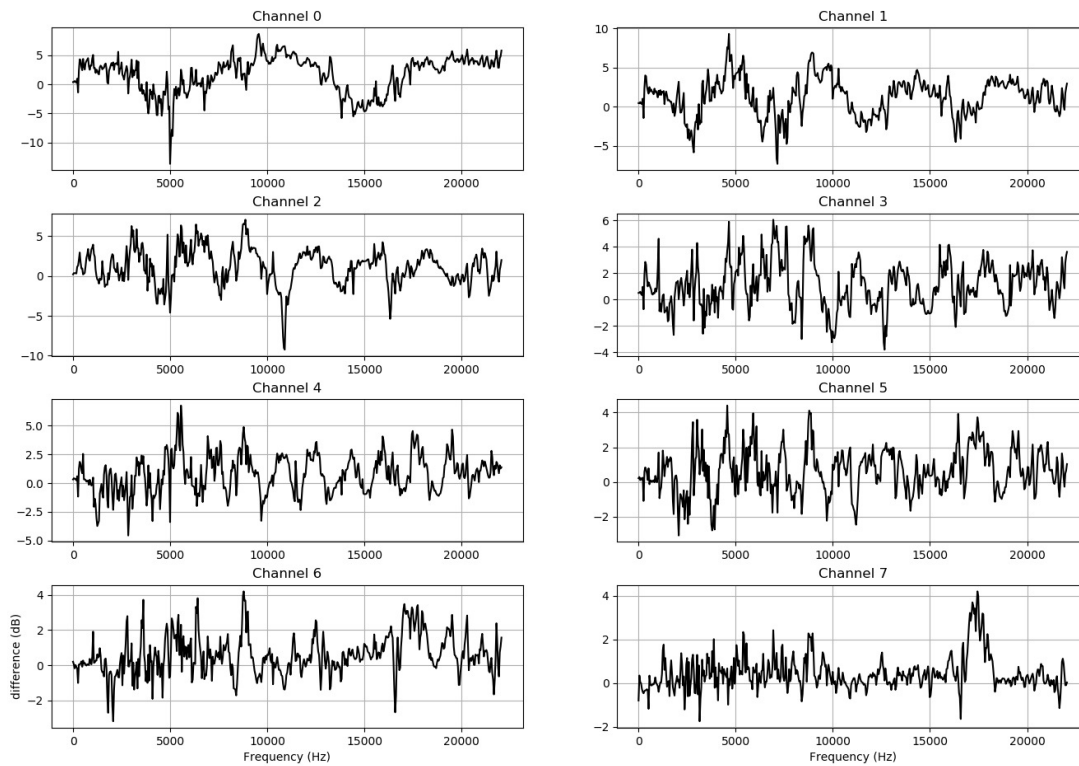


Fig. 18—Power spectral density dB difference between wall present (Channel 0 is 0.0173 m from the wall) and wall removed curves.

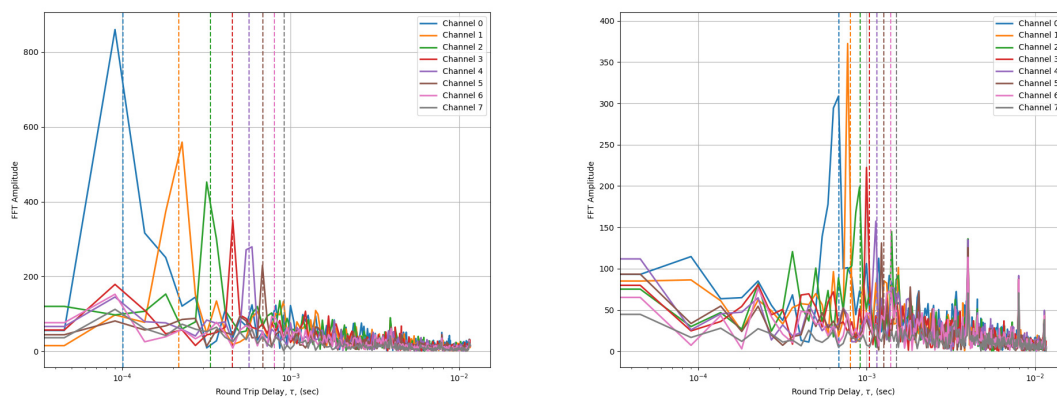


Fig. 19—Plot of spectral content showing time delay estimate and amplitude of spectral peaks for all 8 microphone channels. The vertical dashed lines are the expected time delays based on the measured wall position. (Left) Distance from Channel 0 to wall is 0.0173 m, (Right) Distance from Channel 0 to wall is 0.117 m.

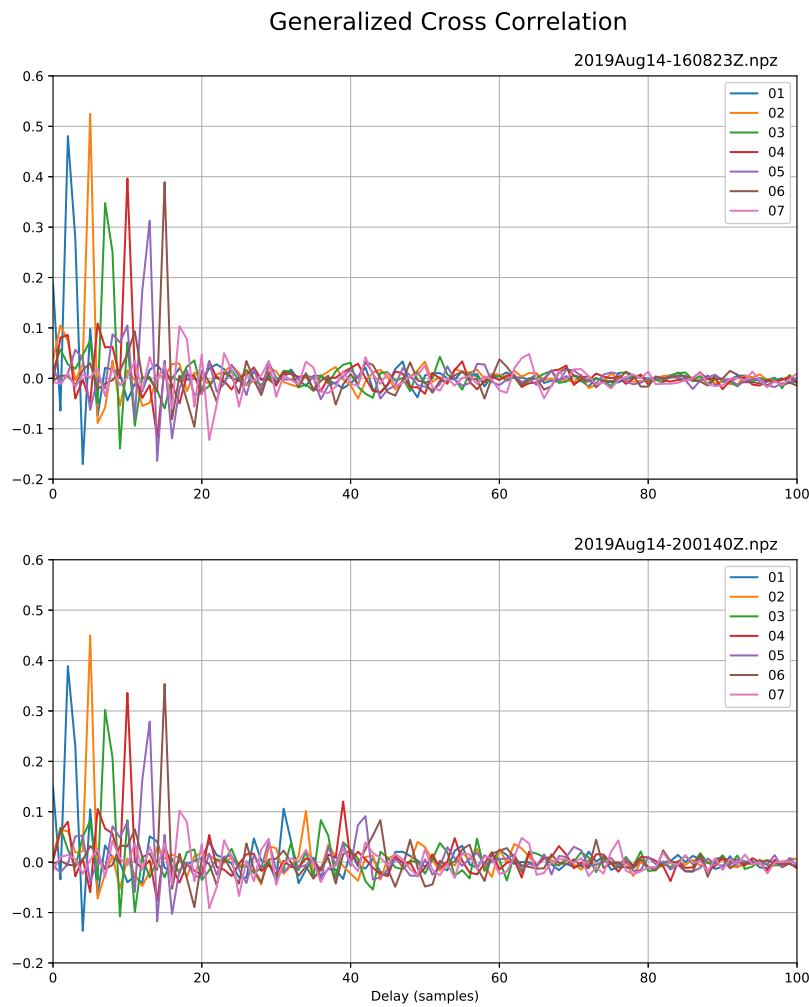


Fig. 20— Generalized cross correlation between Channel 0 (array Channel 0 is closest to wall) and array Channels (1 - 7). The cross correlations are formed from averaging 10 snapshots of 4096 samples with 50% overlap (approximately 0.5 seconds of data). (Top) Wall removed, (Bottom) Wall is 0.117 m from Channel 0. The top plot shows peaks at the direct path arrivals, and the bottom shows both the direct path and weaker reflected arrivals delayed in time.

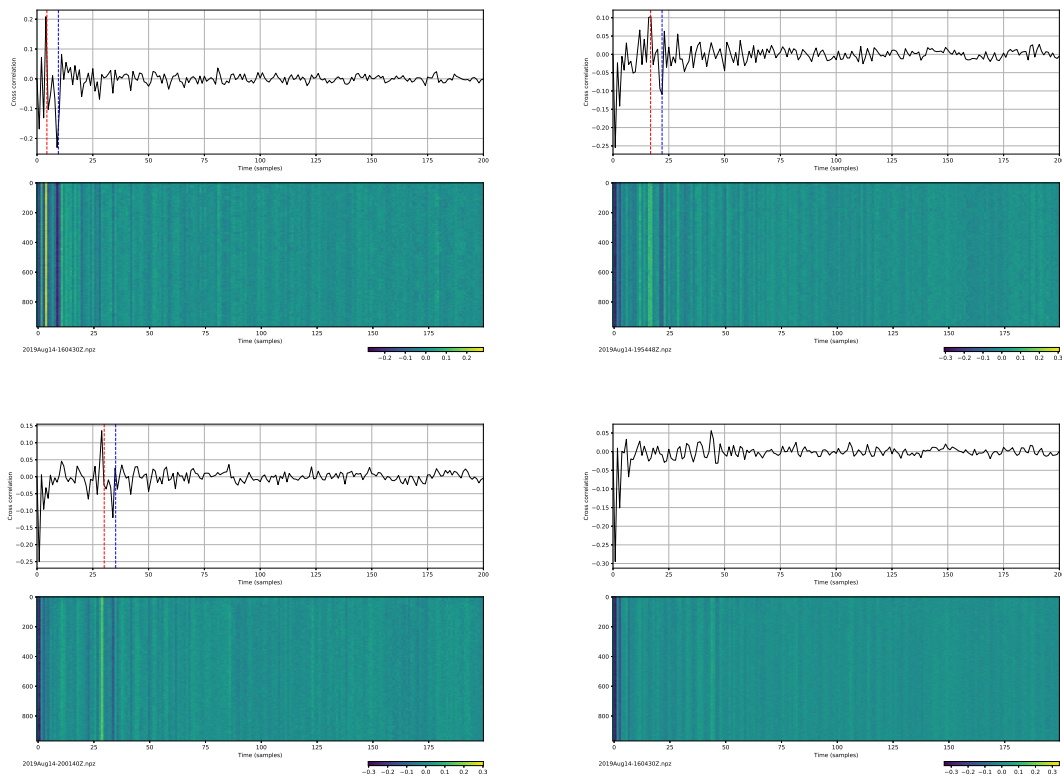


Fig. 21— Acoustic data from Channels 0, 1 (array Channel 0 is closest to wall) is processed with the generalized cross-correlation processor given in Equation 5. The four frames correspond to different distances between Channel 0 and the wall. (Upper Left) 0.017 m, (Upper Right) 0.066 m, (Lower Left) 0.117 m, and (Lower Right) no wall. For each frame the upper plot is an average of the cross-correlation over the entire data set (over 1.5 minutes) with the Channel 0, 1 time-delays shown as dashed vertical lines. The lower color figures show a stacking of the cross-correlations at 0.1 second intervals. The cross-correlation approach can recover the reflection delays in the 0.1 second intervals.

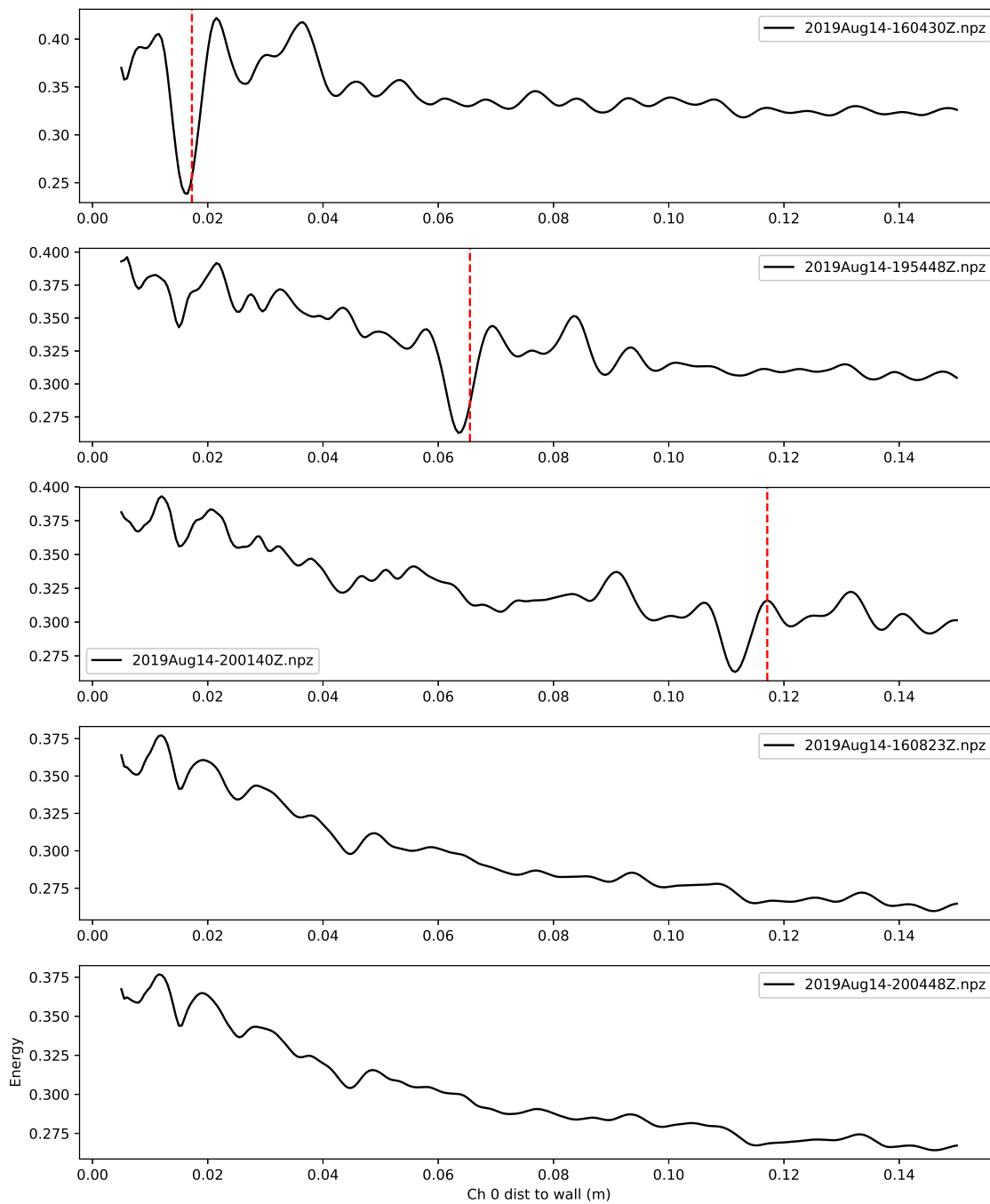


Fig. 22— Acoustic data from Channels 0, 1 (two channels closest to wall) of the linear array were used to estimate the Channel 0 to wall distance with the optimization given in Equation 6. The plots show the optimization for the Channel 0 to wall distance at the minimum of an energy functional defined $E = 1 - J$. Four different cases were measured: corresponding to Channel 0 distances to the reflecting wall of 0.017, 0.066, 0.117 m, and two trials with the wall removed. The red dashed vertical line in the top three plots shows the actual Ch 0 to wall distances, and the bottom two are for the no wall test cases. A minimum in the cost function occurs near the measured value with a bias that increases with increasing distance from the wall.

ACKNOWLEDGMENTS

This would was supported by the Naval Research Laboratory through a Naval Innovative Science and Engineering funded program. The authors would like to thank our collaborators at the U.S. Air Force Research Laboratory, Ryan Kramer, and the U.K. Defence Science and Technology Laboratory, Andrew Evans.

REFERENCES

1. A. Boonman, S. Bumrungsri, and Y. Yovel, “Nonecholocating Fruit Bats Produce Biosonar Clicks with their Wings,” *Current Biology* **24**(24), 2961–2967 (2014).
2. E. Munch, “A user’s guide to topological data analysis,” *Journal of Learning Analytics* **4**(2), 47–61 (2017).
3. Y. T. Cho, “Characterizing Sources of Small DC Motor Noise and Vibration,” *Micromachines* **9**(2), 84 (2018).
4. H. J. Lee, S. U. Chung, and S. M. Hwang, “Noise Source Identification of a BLDC Motor,” *Journal of Mechanical Science and Technology* **22**, 708–713 (2008).
5. C. H. Knapp and G. C. Carter, “The Generalized Correlation Method for Estimation of Time Delay,” *IEEE Transactions on Acoustics, Speech and Signal Processing* **24**(4), 320–327 (1976).

This page
intentionally
left blank

Appendix A

MODELING ATTENUATION

The purpose of the attenuation model is to predict how the environment effects the motor signal propagation in air. Transmitted pulses are affected by ambient temperature, relative humidity, carrier frequency, and transmitter sound pressure level. This model assumes that the only modes of acoustic attenuation in air are spreading losses and atmospheric attenuation. The attenuation is quantified using

$$A_T = 20g \log_{10} \frac{r_2}{r_1} + ar_2 \quad (A1)$$

where the first component describes spherical losses and the second represents atmospheric losses. As the acoustic pulse travels away from the transmitter the pulse intensity decreases due to physical spreading where r_2/r_1 where r_1 is a reference distance, g is a constant based on the geometry of wave propagation. The absorption coefficient, a , quantifies the loss in sound pressure level (SPL) intensity due to the atmosphere and is a function of frequency, temperature and water vapor concentration. The international organization for standardization (ISO) 9613-1:1996 has developed an empirical model that defines the magnitude of the attenuation.

Air attenuates the acoustic signal by two phenomenon; viscous losses due to friction between air molecules (proportional to the square of the frequency) and relaxational processes where air molecules absorb sound energy in the form of vibrations and rotations. This energy is re-radiated in a way that can interfere with other incoming sound and is highly dependent on relative humidity. Figure A1 plots the relationship between the absorption coefficient, temperature, and relative humidity for several frequencies that are applicable to this research.

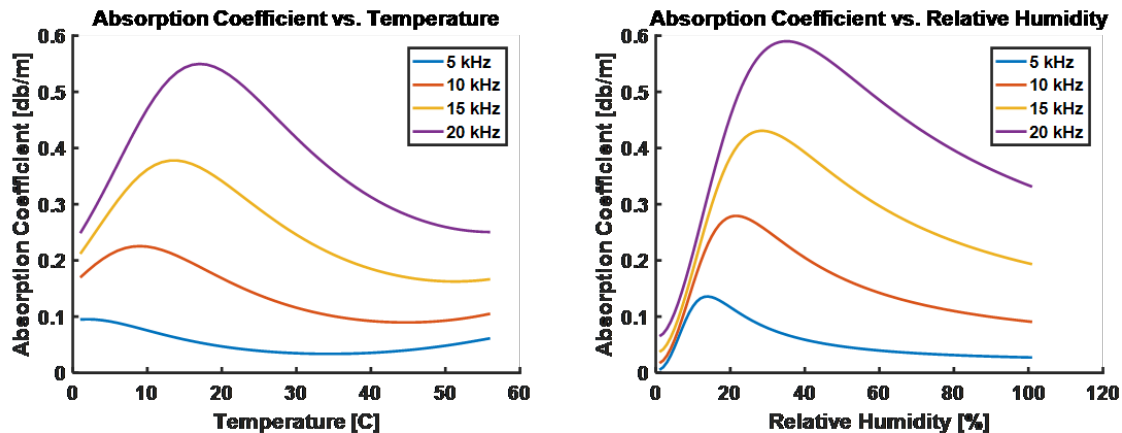


Fig. A1—(Left) Temperature and (Right) relative humidity effects on attenuation.

Signal to noise ratio (SNR) compares the strength of the signal at a given distance from the source, to the magnitude of the noise floor. The pulse strength must be above the noise floor to be detectable.

An SNR less than one indicates that the signal pulse has become quieter than ambient noise and therefore would require special signal processing techniques in order for detection. Using the modeled attenuation and measurements of the noise floor and SPL emitted by the motor the SNR can be calculated and plotted for varying distances as shown in Figure A2.

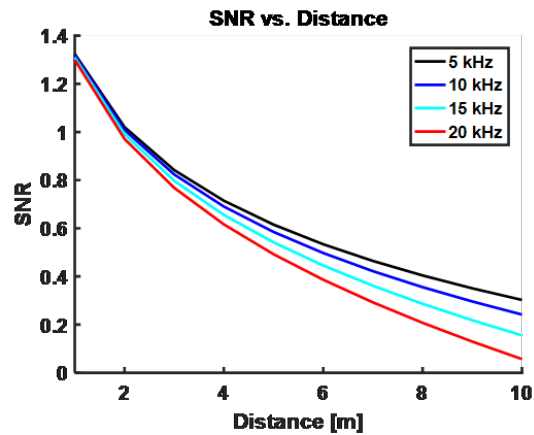


Fig. A2—Signal to noise ratio for several switching frequencies of a small brushed motor.

The SNR for several different switching frequencies remain above the noise floor for 10 meters. This shows that exploiting these signals for environment sensing in close quarters is feasible.

Appendix B

MEASUREMENT SUMMARY

B.1 January 22, 2019 - 6 mm motor tests

Location: LASR high bay west

Vehicle Platform: Statically mounted 6 mm motor, with 3 blade propeller

Microphone Configuration: 8 channel, 44.1 kHz sample rate, linear array oriented end fire to the vehicle rotor. Channel 0 closest, channel 7 furthest. Microphones are equally spaced at 10 cm, with channel 0 approximately 10 cm from propeller.

Testing notes: Collect 1 minute segment of data for the following configurations. Wind screens on microphones for all measurements except the last four (*).

Table B1—January 22, 2019 acoustic measurements

Time (Z)	Duty Cycle	PWM Frequency (Hz)	Time (Z)	Duty Cycle	PWM Frequency (Hz)
165910	0.5	350	210336	0.5	750
170040	0.5	500	210452	0.5	1600
170227	0.5	750	210610	0.75	350
170355	0.5	1600	210727	0.75	500
170527	0.75	350	210848	0.75	750
170711	0.75	500	211002	0.75	1650
170834	0.75	750	211120	0.25	350
170950	0.75	1600	211238	0.25	500
171112	0.25	350	211354	0.25	750
171230	0.25	500	211512	0.25	1600
171348	0.25	750	*212016	0.5	350
171508	0.25	1600	*212141	0.5	500
210110	0.5	350	*212257	0.5	750
210222	0.5	500	*212410	0.5	1600

B.2 January 24, 2019 - 6 mm motor tests

Location: LASR high bay west

Vehicle Platform: Statically mounted 6 mm motor, with 3 blade propeller, same configuration as January 22, 2019.

Microphone Configuration: PDSU Node 1, 8 acoustic channels, 44.1 kHz sample rate, linear array oriented endfire to the vehicle rotor. Channel 0 closest, channel 7 furthest. Microphones are equally spaced at 10 cm, with channel 0 approximately 10 cm from propeller. Wind screens are not on microphones.

Testing notes: Collect 1 minute segment of data for the following configurations. For the PWM frequencies below there is a calibrated value and a nominal value (in parenthesis).

Table B2—January 24, 2019 acoustic measurements

Time (Z)	Duty Cycle	PWM Frequency (Hz)	Note
162404	0.75	1546 (1600)	heavy rain is heard outside
163851	0.75	(1600)	
164502	0.50	(1600)	
171714	0.75	(1600)	
173858	0.75	1236 (1500)	15 sec collect, propeller removed from motor $v = 1.87$
174058	0.75	1030 (1200)	$v = 1.87$ (windy outside)
174320	0.75	883 (1000)	$v = 1.86$
174524	0.75	(1600)	
175024	0.50	800/1600	Trial 1, SOS sequence using 2 PWM frequencies
175708	0.50	800/1600	Trial 2, SOS sequence using 2 PWM frequencies

B.3 January 25, 2019 - 4 and 8 mm motor tests

Location: LASR high bay west

Microphone Configuration: PDSU Node 1, 4 channel, 44.1 kHz sample rate, linear array oriented endfire to the vehicle rotor. Channel 0 closest, channel 3 furthest. Microphones are equally spaced at 10 cm, with channel 0 approximately 10 cm from propeller.

Vehicle Platform: Statically mounted motors of variable sizes (8mm motor with 3 blade prop, 4 mm motor with 2 blade prop).

Notes for 8 mm motor tests: Collect 30 sec segments of data for the following configurations, wind screens not on microphones. Times are the acoustic data timestamp. Today oscilloscope was hooked to PWM to directly measure PWM voltage and frequency.

Table B3—January 25, 2019 8mm motor acoustic measurements

Time (Z)	Duty Cycle	Voltage (V)	PWM (Hz)	Time (Z)	Duty Cycle	Voltage (V)	PWM (Hz)
153810	.25	0.517	1543	155944	.50	1.17	686
153947	.25	0.516	1236	160912	.50	1.22	441
154130	.25	0.498	1031	161015	.50	1.12	326
154328	.25	0.479	882	161122	.75	1.82	1545
154450	.25	0.516	687	161240	.75	1.83	1238
154630	.25	0.518	442	161334	.75	1.81	1031
154744	.25	0.495	326	161432	.75	1.81	884
155104	.50	1.160	1545	161533	.75	1.81	687
155206	.50	1.190	1238	161630	.75	1.86	442
155401	.50	1.140	1030	161735	.75	1.75	326
155517	.50	1.140	884				

Notes for 4 mm motor tests: 2 blade propeller, 30 sec data collections. Motor died on trial at 165210 and was replaced. Acoustic output looked cleaner after motor was replaced.

Table B4—January 25, 2019 4 mm motor measurements

Time (Z)	Duty Cycle	Voltage (V)	PWM (Hz)	Time (Z)	Duty Cycle	Voltage (V)	PWM (Hz)
163040	0.25	0.863	1543	164515	0.50	1.84	686
163211	0.25	0.864	1235	164625	0.50	2.00	441
163331	0.25	0.806	1030	164725	0.50	1.76	325
163430	0.25	0.775	882	164915	0.75	2.81	1543
163530	0.25	0.850	686	165210	0.75	xxxx	xxxx
163625	0.25	0.878	441	171540	0.75	2.72	1235
163803	0.25	0.878	441	171700	0.75	2.69	1029
163920	0.25	0.820	325	171815	0.75	2.68	883
164022	0.50	1.780	1543	171925	0.75	2.68	686
164143	0.50	1.830	1235	172025	0.75	2.79	441
164240	0.50	1.740	1029	172125	0.75	2.55	325
164337	0.50	1.750	882				

B.4 February 25, 2019, 8.5 mm motor measurements

Location: LASR Anechoic Chamber

Microphone Configuration: Description is incomplete for this data set. PDSU Node 1, 4 channel, 44.1 kHz sample rate, linear array. I believe this is the same geometry as February 27 and 28, 2019 which was 0.10 m channel spacing with propeller mounted in center between channels 1 and 2.

Vehicle Platform: Statically mounted 8.5 mm motor with 3 bladed propeller. The 8.5 mm motor is easily confused with the 8 mm motor. The 8.5 mm motor has a hole in top.

Testing notes: The propeller rotation rate was measured with a hand held tachometer.

Table B5—February 25, 2019 8.5 mm motor tachometer measurements

Duty Cycle	PWM (Hz)	Blade Passage Rate (BPM)
8	1000	25400
25	1000	45300
60	1000	65000

Table B6—February 25, 2019 8.5 mm motor acoustic measurements

Time (Z)	Duty Cycle	PWM (Hz)	Time (Z)	Duty Cycle	PWM (Hz)
195713	.08	1031	202347	0.60	9000
195812	.08	1543	202428	0.60	8000
195917	.08	5000	202500	0.60	7000
200013	.08	10000	202533	0.60	6000
200204	.25	1031	202637	0.60	5000
200258	.25	1543	202915	0.60	10000
200349	.25	5000	203050	0.50	10000
200449	.25	10000	203132	0.40	10000
200618	.60	1031	203206	0.30	10000
200707	.60	1543	203249	0.20	10000
200800	.60	5000	203332	0.10	10000
200900	.60	10000	203635	0.60	15000
202315	.60	10000	203820	0.60	20000

B.5 February 27, 2019, 4 mm, 6 mm and 8 mm motor measurements

Location: LASR Anechoic Chamber

Microphone Configuration: PDSU Node 1, 4 channel, 44.1 kHz sample rate, linear array; 0.10 m channel spacing with propeller mounted in center between channels 1 and 2.

Vehicle Platform: Statically mounted 6 mm and 8 mm motor with 3 bladed propeller. The 4 mm motor had a 2 bladed propeller.

Testing notes: The propeller rotation rate was measured with a handheld tachometer. PWM frequencies in parenthesis are nominal values (not measured on oscilloscope). 30 sec data collects. For the 6 mm motor the propeller started flying off during the 0.60 duty cycle measurements. The two columns of tachometer measurements for the 8 mm motor correspond to before and after the test. The battery voltage at the end of the test was 3.85 V, it was not recorded at the beginning of the test.

Table B7—February 27, 2019 6 mm motor tachometer measurements

Duty Cycle	PWM (Hz)	Blade Passage Rate (BPM)
8	1000	17700
25	1000	32300
60	1000	48000

Table B8—February 27, 2019 6 mm motor acoustic measurements

Time (Z)	Duty Cycle	PWM (Hz)	Voltage (V)
155745	.08	1027 (1031)	0.220
155910	.08	(1543)	
160340	.08	4900 (5000)	0.225
161346	.08	(10000)	0.226
161502	.25	1024 (1031)	0.705
161600	.25	1580 (1543)	0.655
161754	.25	4900 (5000)	0.615
161911	.60	1024 (1031)	1.450

Table B9—February 27, 2019 8 mm motor tachometer measurements

Duty Cycle	PWM (Hz)	Blade Passage Rate (BPM)
8	1000	24900, 23400
25	1000	48000, 45700
60	1000	70000, 67000

Table B10—February 27, 2019 8 mm motor acoustic measurements

Time (Z)	Duty Cycle	PWM (Hz)	Voltage (V)
171230	.08	1024 (1031)	0.525
171319	.08	1580 (1543)	0.475
171409	.08	4900 (5000)	0.515
171554	.08	4970 (10000)	0.489
171913	.25	1026 (1031)	1.16
172002	.25	1523 (1543)	1.15
172056	.25	4900 (5000)	1.02
172157	.25	10000 (10000)	1.08
172308	.60	1026 (1031)	1.85
172406	.60	1523 (1543)	1.86
172512	.60	4900 (5000)	1.79
172627	.60	11100 (10000)	1.75
173118	.60	(10000)	
173205	.60	(9000)	
173240	.60	(8000)	
173328	.60	(7000)	
173407	.60	(6000)	
173525	.60	(5000)	
173612	.60	(15000)	
173717	.60	(20000)	

Table B11—February 27, 2019 4 mm motor tachometer measurements

Duty Cycle	PWM (Hz)	Blade Passage Rate (BPM)
8		17900
25		35600
60		53000

Table B12—February 27, 2019 4 mm motor acoustic measurements

Time (Z)	Duty Cycle	PWM (Hz)	Voltage (V)	Note
195745	.08	1027 (1031)	0.465	
195835	.08	1520 (1543)	0.411	
195920	.08	4900 (5000)	0.490	
200042	.08	4900 (10000)	0.475	
200201	.25	1025 (1031)	1.31	
200245	.25	1522 (1543)	1.23	
200336	.25	4900 (5000)	1.14	
200442	.25	10520 (10000)	1.24	
200550	.60	1025 (1031)	2.5	
200755	.60	4900 (5000)	2.44	
200850	.60	(10000)		
201019	.60	(10000)		
201052	.60	(9000)		
201141	.60	(8000)		
201311	.60	(7000)		
201410	.60	(6000)		
201510	.60	(5000)		
201618	.60	(15000)		
201656	.60	(20000)		
203444	.60	(5000)		Wall placed at end of rod
203636	.60	(5000)		Wall removed

B.6 February 28, 2019, 8.5 mm motor measurements

Location: LASR Anechoic Chamber

Microphone Configuration: PDSU Node 1, 4 channel, 44.1 kHz sample rate, linear array; 0.10 m channel spacing with propeller mounted in center between channels 1 and 2.

Vehicle Platform: Statically mounted 8.5 mm motor with 3 bladed propeller

Testing notes: A series of tests including wall/no-wall tests with the wall perpendicular and parallel to the microphone array axis. For the wall parallel to array axis, it is displaced from the array axis by 0.20 m, and the propeller is between Channels 1 and 2, at .03 m on the opposite side of the array. Also measurements of duty cycle and PWM frequency sweeps. Nominal PWM frequency is in parenthesis.

Table B13—February 28, 2019 with wall perpendicular to array axis (left column) an no-wall (right column) measurements

Time (Z)	Duty Cycle	PWM (Hz)	Voltage (V)	Time (Z)	Duty Cycle	PWM (Hz)	Voltage (V)
155000	.60	4900 (5000)	1.76	160130	.60	4900 (5000)	1.70
155223	.60	11200 (10000)	1.74	160305	.60	10600 (10000)	1.70
155307	.60	8800 (9000)	1.74	160355	.60	8700 (9000)	1.70
155404	.60	(8000)	1.72	160444	.60	(8000)	1.70
155505	.60	7300 (7000)	1.70	160525	.60	7400 (7000)	1.65
155607	.60	6300 (6000)	1.68	160616	.60	6300 (6000)	1.65
155708	.60	4900 (5000)	1.69	160652	.60	4900 (5000)	1.68
155755	.60	14700 (15000)	1.54	160737	.60	14700 (15000)	1.50
155830	.60	20800 (20000)	1.57	160819	.60	20300 (20000)	1.53

Table B14—February 28, 2019 with wall parallel to array axis

Time (Z)	Duty Cycle	PWM (Hz)	Voltage (V)	Time (Z)	Duty Cycle	PWM (Hz)	Voltage (V)
162415	.60	4900 (5000)	1.70	162744	.60	6300 (6000)	1.64
162510	.60	11100 (10000)	1.68	162837	.60	4900 (5000)	1.65
162550	.60	8800 (9000)	1.69	162922	.60	14700 (15000)	1.50
162627	.60	(8000)	1.67	162959	.60	20400 (20000)	1.53
162710	.60	7300 (7000)	1.65				

Table B15—February 28, 2019 PWM sweeps

Start Time (Z)	Stop Time (Z)	Duty Cycle	PWM (Hz)
170332	171235	.08	5000 - 15000
172945	173815	.25	5000 - 15000
173909	174739	.60	5000 - 15000
190812	191643	.50	5000 - 15000

Table B16—February 28, 2019 duty cycle sweeps

Start Time (Z)	Stop Time (Z)	Duty Cycle	PWM (Hz)
191810	191919	0.01 - 0.99	7000
191950	192100	0.01 - 0.99	12000
192141	192251	0.01 - 0.99	3500

B.7 April 9, 2019, 4 mm motor measurements

Location: LASR Anechoic Chamber

Microphone Configuration: PDSU Node 1, 4 channel, 44.1 kHz sample rate, linear array; 0.10 m channel spacing with propeller mounted in center between channels 1 and 2.

Vehicle Platform: Statically mounted 4 mm motor with 2 bladed propeller.

Testing notes: A series of tests including sweeps with and without wall perpendicular to the microphone array axis. During this test we discovered that in previous tests, the 4 mm motor thrust may have been reversed, because there are two oppositely spinning motor types and two 2 bladed propeller types. Chirp tests (changing the PWM frequency between two discrete values (100 Hz for remainder, and 12000 Hz for 1 ms) with 5 sec repetition rate were also performed.

Table B17—April 9, 2019 PWM and duty cycle sweeps without wall

Start Time (Z)	Stop Time (Z)	Duty Cycle	PWM (Hz)
154700	155524	.60	5000 - 15000
155715	160537	.25	5000 - 15000
161128	161230	0.01 - 0.99	11000
161330	161423	0.01 - 0.99	6000

Table B18—April 9, 2019 wall tests

Time (Z)	Duty Cycle	PWM (Hz)	Ch 0 wall distance (m)
185749	.60	5000	0.129
190019	.80	5000	0.129
190115	.25	5000	0.129
191055	.60	5000	0.315
191210	.80	5000	0.315
191312	.25	5000	0.315
191705	.60	5000	0.222
191750	.80	5000	0.222
191838	.25	5000	0.222
192122	.60	5000	0.145
192223	.80	5000	0.145
192310	.25	5000	0.145
192632	.60	5000	0.098
192720	.80	5000	0.098
192818	.25	5000	0.098
193443	.60	5000 - 15000	0.098
194400	.25	5000 - 15000	0.098
195402	0.01 - 0.99	6000	0.098
195556	0.01 - 0.99	11000	0.098
200059	0.60	5000 - 15000	0.316
200950	0.25	5000 - 15000	0.316
201857	0.01 -0.99	6000	0.316
202020	0.01 -0.99	11000	0.316

B.8 April 10 - 11, 2019, 4 mm and 8.5 mm motor measurements

Location: LASR Anechoic Chamber

Microphone Configuration: PDSU Node 1, 4 channel, 44.1 kHz sample rate, linear array.

Vehicle Platform: Statically mounted 4 mm motor with 2 bladed propeller was used on April 10, the 4 mm and 8.5 mm motors were used on April 11.

Testing notes for April 10, 2019: See lab book notes for more details. On these dates we ran a series of tests with the wall parallel and perpendicular to the array axis. The measurement references were changed midway through the testing, and there is a note about changing from white to black propeller midway through the testing (to reverse the direction of thrust).

Testing notes for April 11, 2019: Chirp tests (changing the PWM frequency between two discrete levels) were performed (see lab book for more detail). Initial analysis of this data showed no detectable reflection from a wall. These test may be revisited at some point to refine the pulse timing and the wall distances.

B.9 June, 14 2019 - 8 mm motor tests

Location: In LASR lab outside anechoic chamber

Vehicle Platform: Statically mounted 8 mm motor, with 3 blade propeller

Channel Configuration: 8 channels, 44.1 kHz sample rate. Channels 0 -3 linear microphone array as shown in Figure 2, Channels 4 - 6 were non-acoustic data channels: power to motor, piezo-electric transducer underneath motor support structure, and PWM command signal to electronic motor driver. Channel 0 is closest to the removable wall location. Microphones are equally spaced at 0.10 m, with the propeller equidistant between Channels 1 and 2.

Testing notes: 50 percent duty cycle was used on all runs. Three different PWM signals were measured: constant 5 kHz, 5 s-up/ 5 s-down triangle ramp between 5 - 10 kHz, and 1 s-up/ 1 s-down triangle ramp between 5 - 10 kHz. The removable wall was places 0.105 m from Channel 0.

Table B19—June 14, 2019 measurements

Time (Z)	Description
134020	Constant 5 kHz PWM for 30 seconds, wall in place
134112	Triangle PWM sweep 5 - 10 kHz (5 sec-up, 5 sec-down), wall in place
134439	Triangle PWM sweep 5 - 10 kHz (1 sec-up, 1 sec-down), wall in place
134657	Constant 5 kHz PWM, no wall
134805	Triangle PWM sweep 5 - 10 kHz (5 sec-up, 5 sec-down), no wall
135128	Triangle PWM sweep 5 - 10 kHz (1 sec-up, 1 sec-down), no wall

B.10 August, 14 2019 - 8 mm motor tests

Location: LASR desert high bay

Vehicle Platform: Statically mounted 8 mm motor, with 3 blade propeller mounted at one end of 8-channel linear microphone array.

Microphone Configuration: 8 channel, 44.1 kHz sample rate, linear array with uniform 0.02 m spacing. Distance from propeller to microphone Channel 7 is 0.0259 m. The normal of a removable plywood wall with configurable distance as shown in Figure 17 is placed at the Channel 0 end of the array.

Testing notes: Collect 1.5 minute data segments of ambient (motor off) and motor on, with variable wall positions. For all the tests, we use PWM update frequency of 5 kHz, and 50% duty cycle. The wall locations in the table below are referenced from the end of the microphone support rod.

Table B20—August 14, 2019 measurements

Time (Z)	Duty Cycle	PWM Frequency (Hz)	Note
160430	0.5	5000	Wall at .0017 m, Channel 0 wall distance is 0.017 m
160823	0.5	5000	Wall removed
195448	0.5	5000	Wall at 0.05 m, Channel 0 wall distance is 0.066 m
200140	0.5	5000	Wall at 0.102 m, Channel 0 wall distance is 0.117 m
200448	0.5	5000	Wall removed

B.11 August, 15 2019 - 8 mm motor tests

Location: LASR desert high bay

Vehicle Platform: Statically mounted 8 mm motor, with 3 blade propeller mounted at center of circular microphone array.

Microphone Configuration: 6 channel, 44.1 kHz sample rate, circular array. Microphones are mounted along circumference of array; evenly spaced (60 degree separation) and approximately 0.258 m from the motor. The microphone stations around the circumference are A, C, F, H, J, M. The microphone channels are 0 - 5.

Testing notes: Collect 2 minute data segments of ambient (motor off) and motor on, and with microphones rotated in two configurations

Table B21—August 15, 2019 measurements

Time (Z)	Duty Cycle	PWM Frequency (Hz)	Note
150700	0.5	5000	Motor on, Channel assignments 0-A, 1-C, 2-F, 3-H, 4-J, 5-M
150920	0.5	5000	Motor off, Channel assignments 0-A, 1-C, 2-F, 3-H, 4-J, 5-M
182030	0.5	5000	Motor on, Channel assignments 0-C, 1-F, 2-H, 3-J, 4-M, 5-A
182256	0.5	5000	Motor off, Channel assignments 0-C, 1-F, 2-H, 3-J, 4-M, 5-A